

AD \_\_\_\_\_

AWARD NUMBER: W81XWH-07-1-0457

TITLE: Magnetic Nanoparticle-Based Imaging of RNA Transcripts in Breast Cancer Cells

PRINCIPAL INVESTIGATOR: Andrew Tsourkas

CONTRACTING ORGANIZATION: University of Pennsylvania  
Philadelphia, PA 19104

REPORT DATE: June 2009

TYPE OF REPORT: Annual

PREPARED FOR: U.S. Army Medical Research and Materiel Command  
Fort Detrick, Maryland 21702-5012

DISTRIBUTION STATEMENT: Approved for Public Release;  
Distribution Unlimited

The views, opinions and/or findings contained in this report are those of the author(s) and should not be construed as an official Department of the Army position, policy or decision unless so designated by other documentation.

REPORT DOCUMENTATION PAGE				Form Approved OMB No. 0704-0188	
Public reporting burden for this collection of information is estimated to average 1 hour per response, including the time for reviewing instructions, searching existing data sources, gathering and maintaining the data needed, and completing and reviewing this collection of information. Send comments regarding this burden estimate or any other aspect of this collection of information, including suggestions for reducing this burden to Department of Defense, Washington Headquarters Services, Directorate for Information Operations and Reports (0704-0188), 1215 Jefferson Davis Highway, Suite 1204, Arlington, VA 22202-4302. Respondents should be aware that notwithstanding any other provision of law, no person shall be subject to any penalty for failing to comply with a collection of information if it does not display a currently valid OMB control number. PLEASE DO NOT RETURN YOUR FORM TO THE ABOVE ADDRESS.					
1. REPORT DATE 1 June 2009		2. REPORT TYPE Annual		3. DATES COVERED 1 Jun 2008 – 31 May 2009	
4. TITLE AND SUBTITLE  Magnetic Nanoparticle-Based Imaging of RNA Transcripts in Breast Cancer Cells				5a. CONTRACT NUMBER	
				5b. GRANT NUMBER W81XWH-07-1-0457	
				5c. PROGRAM ELEMENT NUMBER	
6. AUTHOR(S)  Andrew Tsourkas  E-Mail: atsourk@seas.upenn.edu				5d. PROJECT NUMBER	
				5e. TASK NUMBER	
				5f. WORK UNIT NUMBER	
7. PERFORMING ORGANIZATION NAME(S) AND ADDRESS(ES)  University of Pennsylvania Philadelphia, PA 19104				8. PERFORMING ORGANIZATION REPORT NUMBER	
9. SPONSORING / MONITORING AGENCY NAME(S) AND ADDRESS(ES) U.S. Army Medical Research and Materiel Command Fort Detrick, Maryland 21702-5012				10. SPONSOR/MONITOR'S ACRONYM(S)	
				11. SPONSOR/MONITOR'S REPORT NUMBER(S)	
12. DISTRIBUTION / AVAILABILITY STATEMENT Approved for Public Release; Distribution Unlimited					
13. SUPPLEMENTARY NOTES					
14. ABSTRACT We have developed a novel approach to detect RNA transcripts via magnetic resonance by taking advantage of the decrease in the spin-spin (i.e. T2) relaxation time that results from the self-assembly of superparamagnetic iron oxide nanoparticles (NPs). Specifically, two unique NP-oligonucleotide (ON) conjugates were designed to recognize adjacent sites on nucleic acid targets (Figure 1). Thus, upon hybridization to complementary targets the NP-ON conjugate pairs were brought into close proximity, which resulted in a detectable reduction in the T2 relaxation time. This mechanism of switching from a high T2-relaxation time to a low T2-relaxation time is generally referred to as magnetic relaxation switching (MRSw). We tested the ability of NP-ON conjugates with sizes ranging from ~20 nm to 1 um to detect nucleic acid targets. It was found that aminated NPs ~100 nm in diameter performed the best, exhibiting as much as a 61% decrease in T2 signal upon the addition of nucleic acid targets, with a lower detection limit of 10 pmoles. It was also found that the 100 nm particles were rapidly internalized into cells, opening up the possibility of detecting endogenous RNA.					
15. SUBJECT TERMS Iron oxide nanoparticles, RNA, detection, sensor					
16. SECURITY CLASSIFICATION OF:			17. LIMITATION OF ABSTRACT  UU	18. NUMBER OF PAGES	19a. NAME OF RESPONSIBLE PERSON USAMRMC
a. REPORT U	b. ABSTRACT U	c. THIS PAGE U			19b. TELEPHONE NUMBER (include area code)

## Table of Contents

	<u>Page</u>
Introduction.....	4
Body.....	4
Key Research Accomplishments.....	10
Reportable Outcomes.....	10
Conclusion.....	12
References.....	12
Appendices.....	12

## **INTRODUCTION:**

The goal of the proposed research is to develop a novel approach to image mRNA transcripts via magnetic resonance (MR). Specifically, nucleic acids will be detected by taking advantage of the change in MR contrast that results when two or more superparamagnetic nanoparticles (NPs) are brought into close proximity. The NPs are brought together by designing them such that they bind to adjacent sites on mRNAs that are highly over-expressed in breast cancer cells. The first specific aim of this project involves the synthesis and optimization of magnetic nanoparticle-oligonucleotide (NP-ON) conjugates. In particular, we proposed to synthesize NPs of differing size, magnetic properties, and surface modifications. We then proposed to evaluate which NP configuration allows for the highest sensitivity of RNA detection. Our second specific aim is focused on efficiently delivering NPs into the cytoplasm of breast cancer cells, where they will have access to intracellular mRNA. Of particular interest is the rate and extent of internalization of NPs of varying size and charge. Also, we are interested in the localization of internalized NPs and will explore various endosomal disruption agents to facilitate cytoplasmic delivery. The third aim involves testing whether we can correlate a change in MR contrast to the level of target mRNA in cell lysate and in living breast cancer cells.

## **BODY:**

### **Task 1. To synthesize and optimize magnetic nanoparticle-oligonucleotide (NP-ON) conjugates for detecting nucleic acid targets (Years 1 – 3)**

- a. Synthesize dextran-coated superparamagnetic nanoparticles with amine or carboxyl groups available for conjugation. (Years 1 - 3)

A wide range of nanoparticle (NP) formulations were prepared via the co-precipitation method to generate nanoparticles with varying size, magnetic, and chemical properties. The physical-chemical properties of the NPs were varied by altering the total iron, ratio of ferrous and ferric iron, dextran size and dextran concentration during the synthesis of NPs. All of the NPs were aminated following synthesis to facilitate cellular uptake, without the need for transfection agents (discussed below). Detailed protocols outlining the synthetic procedures for aminated nanoparticles can be found in the appended publication (Thorek et al., 2008).

We have also been able to successfully prepare carboxylated NPs by reacting the aminated nanoparticles with succinic anhydride in an alkaline buffer. Conversion of the amine groups to carboxyl groups was validated by running the NPs on a 1% agarose gel. The carboxylated (i.e. negatively charged) NPs migrated towards the cathode, whereas the aminated NPs migrated towards the anode.

- b. Determine iron-oxide core size, hydrodynamic radius, and relaxivities of the magnetic nanoparticles. (Years 1 - 3)

NPs have been synthesized with hydrodynamic diameters ranging from ~20 nm to ~120 nm. Representative dynamic light scattering (DLS) measurements of nanoparticle diameter are shown in Figure 1. Larger (commercially available) particles with diameters of 200 nm, 300nm, and 1.4 um are also shown in Figure 1. These particles were included in our studies to identify whether

particles larger than 107 nm, which cannot be synthesized by co-precipitation, could be delivered into cells and used to detect endogenous RNA. Similar to the nanoparticles prepared in our lab, the commercial particles were also aminated. A summary of the physical and chemical properties of the SPIO that were evaluated are provided in Table 1.

Interestingly, all of the NPs synthesized in our lab had iron oxide cores of similar size (~6 nm); however, the larger NPs possessed multiple cores (see Figures 2 and 3 in Thorek et al, 2008, attached). Therefore, the larger NPs had a larger “effective” core size. The number of cores ranged from ~1 for the NPs with a ~20 nm hydrodynamic diameter to ~11 for NPs with a hydrodynamic diameter of ~110 nm. The R2 relaxivity increased directly with the NP “effective” core size. For example, a 33 nm NP exhibited an R2 of 71 mM<sup>-1</sup>s<sup>-1</sup>, while a 107 nm NP exhibited an R2 of 381 mM<sup>-1</sup>s<sup>-1</sup>. The R1 values decreased with increasing hydrodynamic diameter, going from 13.56 mM<sup>-1</sup>s<sup>-1</sup> for the 33 nm NPs to 7.24 mM<sup>-1</sup>s<sup>-1</sup> for the 107 nm NPs.

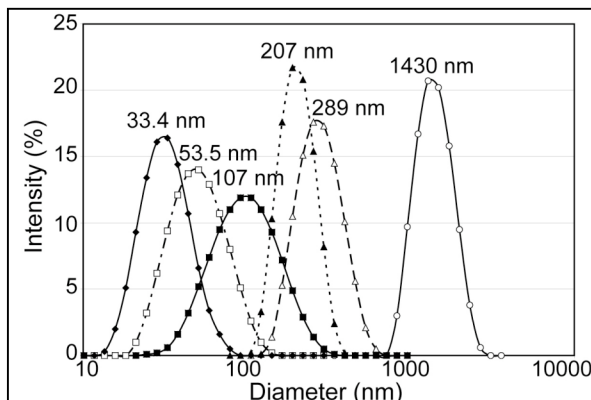


**Figure 1.** Hydrodynamic diameter of SPIO. The hydrodynamic diameter of SPIO particles was determined by DLS. Intensity measurements are reported and the peak intensity is provided for each distribution.

**Table 1.** Physical and magnetic properties of NPs

Hydrodynamic Diameter (nm)	Core Diameter (nm)	Number of cores	R <sub>2</sub> (mM <sup>-1</sup> s <sup>-1</sup> )	R <sub>1</sub> (mM <sup>-1</sup> s <sup>-1</sup> )*	R <sub>2</sub> /R <sub>1</sub>	NH <sub>2</sub> /particle	Fe (atoms) /particle <sup>†</sup>	Coating Material
33	6.067	1.9	71.00	13.56	5.24	185	8924	Dextran
53	5.603	5.3	82.25	9.97	8.25	631	20065	Dextran
107	6.534	11.2	381.00	7.24	52.66	1024	66729	Dextran
207	175.4	1	176.58	0.51	344.48	6.0 x 10 <sup>5</sup>	6.3 x 10 <sup>7</sup>	Styrene Copolymer
289	289.6	1	115.20	0.34	337.43	2.2 x 10 <sup>6</sup>	2.6 x 10 <sup>8</sup>	Styrene Copolymer
1430	-	1	64.32	0.41	156.49	8.5 x 10 <sup>8</sup>	1.3 x 10 <sup>7</sup>	Silica

In addition to preparing dextran coated iron oxide nanoparticles by co-precipitation, we have also synthesized iron oxide nanoparticles via thermal decomposition (Park et al, 2004). This synthetic approach allows for the synthesis of NPs with single iron oxide cores of relatively monodisperse size. The size can also be controlled by varying the synthetic conditions. Thus far, we have made NPs with an iron oxide core diameter of ~5 nm (Figure 2) and 20nm. To make these NPs water-soluble we have seeded a gold coating onto the NP surface. An example transmission electron microscopy image of gold-coated iron oxide NPs is shown in Figure 2.

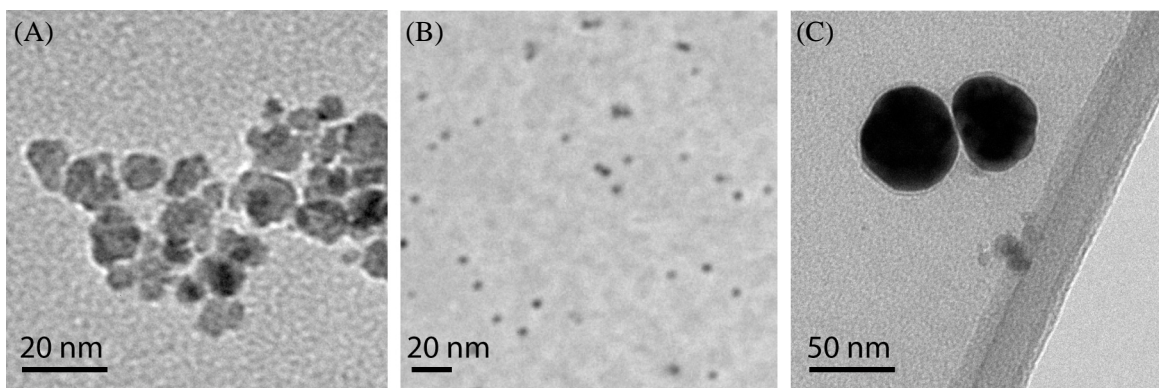


**Figure 2.** Transmission electron microscope images of iron oxide nanoparticles. (A) Dextran-coated iron oxide nanoparticles. TEM images show that the iron oxide cores are heterogeneous in size. (B) Iron oxide nanoparticles prepared by thermal decomposition. TEM images show relatively uniform size distribution of iron oxide cores. (C) TEM image of gold-coated iron oxide nanoparticles.

- c. Use chemical cross-linkers to attach oligonucleotides to the magnetic nanoparticles. Oligonucleotides will be synthesized with a photocleavable linkage. (Years 1 - 3)

We have explored four different approaches for attaching oligonucleotides (ONs) to the NPs. Specifically, the approaches that we have developed include (1) reacting ONs that possess a terminal amine with disuccinimidyl suberate (DSS), precipitating the ON in acetone, and resuspending the ON pellet with aminated, dextran-coated NPs; (2) reacting carboxylated, dextran-coated NPs with EDC and sulfo-NHS, precipitating the NPs in isopropanol, and resuspending in aminated ONs; (3) incubating thiolated ONs with gold coated NPs; (4) using Cu-catalyzed terminal alkyne-azide cycloaddition (CuAAC) to couple alkyne labeled ONs to azide labeled NPs. The number of ONs per NP was easily determined in each case since we labeled each oligonucleotide with a fluorescent dye that could be quantified via absorbance measurements. The number of ONs per NP was typically in the range of 2 to 10 depending on the nanoparticle synthesis protocol and the conjugation procedure.

It should be noted that identical conjugation protocols were used to attach ONs with photocleavable linkages to the NPs. The photocleavable linkage was inserted between the terminal functional group (i.e., sulfhydryl, amine, alkyne) and the first base during oligonucleotide synthesis.

Out of the four conjugation schemes tested, CuAAC was found to be the most efficient, both in terms of the number of ONs per NP and the percent of ONs that were actually conjugated to the NP. This proved to be the case, not only for ON-NP conjugations but also antibody-NP conjugations (Figure 3), which are notoriously difficult to perform due to the large size of both the antibody and NP (Thorek et al, under review, see attached).

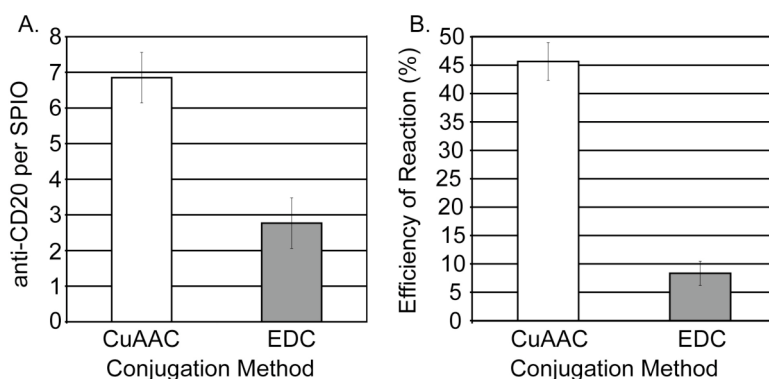


**Figure 3.** Comparison of CuAAC and EDC conjugation procedures. (A) The average number of antibodies per NP was determined to be 6.85 molecules per particle using CuAAC and 2.77 antibodies per NP using EDC. (B) The ratio of final protein per NP with respect to the initial amount of protein used during the conjugation reaction.

- d. Perform hybridization assays with NP-ON conjugates in the presence of varying amounts of nucleic acid targets and record T2 relaxation times before and after UV exposure. Analogous studies will be performed with a mutant (not perfectly complementary) target to serve as a negative control. Targets with a varying number of binding sites and varying spacing between binding sites will also be tested. (Months 4 - 12)

The lower detection limit for nucleic acid detection was determined by serially diluting samples of oligonucleotide targets (1  $\mu\text{M}$  to 1 aM) and mixing them with pairs of NP-ONs that hybridize to adjacent sites on the target DNA. Using 33 nm NP-ONs with an R2 of 71 (mMsec)<sup>-1</sup> and ~3 ONs per NP, we have found that we can detect as little as 10 pmoles of target (Figure 4). Higher target concentrations produced as much as a 41% change in T2 signal (38 ms). Furthermore, the signal reduction was not seen when similar concentrations of a non-specific target was used. We have also tested whether the spacing between NPs on the oligonucleotides target influences our lower detection limit. Specifically, we have tested NP-ON probes that bind to DNA targets with no space

between the hybridized NP-ONs and with a spacing of 6 bases between the hybridized NP-ON. We did not observed any statistical difference in the T2-relaxation times measured when NP-ONs were incubated with these two targets. This is most likely because this single stranded domain most likely forms a random coil and thus does not have a significant impact on the distance between NP-ONs.

To determine the influence of NP size on the lower detection limit, we have also performed RNA detection assays with each of the NPs listed in Table

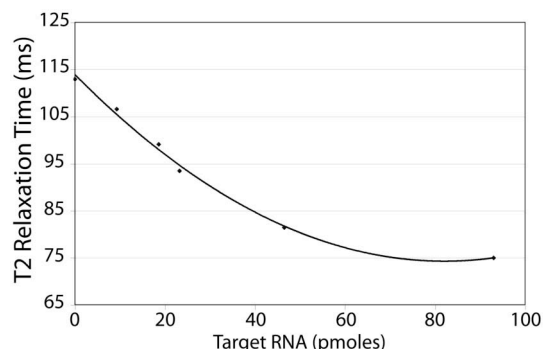


**Figure 4.** Detection of RNA via Magnetic Relaxation Switching. Binding of NP-ONs to adjacent sites on nucleic acid targets led to a dramatic decrease in the T2 relaxation time. The extent of change in the T2 relaxation time correlated directly with target concentration with a maximum reduction (41%) occurring at ~95 pmoles.

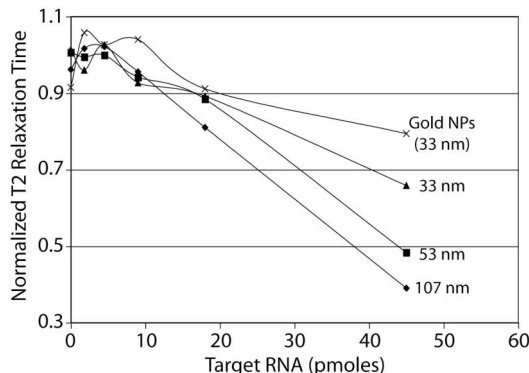


**Figure 5.** Effect of NP size and coating on RNA detection via magnetic relaxation switching.

1 as well as the gold-coated NPs (Figure 5). Upon the addition of target RNA, the larger commercial particles tended to precipitate out of solution making it difficult to acquire repeatable measurements, therefore, this data was excluded from Figure 5. Interestingly, it was found that the larger dextran-coated NPs (i.e. 107 nm) exhibited a greater percent change in T2 relaxation time upon the addition of target RNA compared with the smaller dextran- and gold-coated NPs; however, the lower detection limit did not improve. None of the NP formulations could reliably detect less than 10 pmoles of target RNA.

## **Task 2. To delivery NP-ON conjugates to the cytoplasm of MCF-7 breast cancer cells**

- a. Synthesize nanoparticles that are linked to both oligonucleotides and cell penetrating peptides (pNP-ONs). (Years 2 - 3)

We have synthesized NPs with both cell penetrating peptides and ONs, but we have observed that even when aminated NPs are conjugated to ONs without cell penetrating peptides, they can be efficiently internalized into cells - as long as the NP possesses an overall positive charge (Figure 7 in Thorek, et. al, 2008). This has allowed us to evaluate the cellular uptake of NPs over a continuum of NP sizes ranging from 33 nm to nearly 1.5  $\mu$ m without the added complexity of conjugating peptides (discussed below).

- b. Measure the rate and extent of pNP-ON internalization in MCF-7 breast cancer cells. NP-ONs with no internalizing peptide will be used as a control (Months 12 - 18).

We have analyzed the rate and extent of NP uptake in T cells, MCF-7 breast cancer cells, and NIH3T3 cells. In general, all three cells lines behaved similarly. Specifically, the internalization of NPs < 200 nm in diameter was rapid, reaching a plateau within ~ 1hr (Figure 6a). Further, we found that NPs < 200 nm were taken up by cells more efficiently than larger NPs, i.e. they exhibited lower T2 relaxation times (Figure 6b), with the 107 nm NPs exhibiting the lowest T2 relaxation times. Taking into consideration that the 107 nm particles exhibited higher contrast upon RNA binding (Figure 5) and the highest cellular contrast following cellular uptake (Figure 6b), these NPs will be used for all subsequent RNA detection studies.



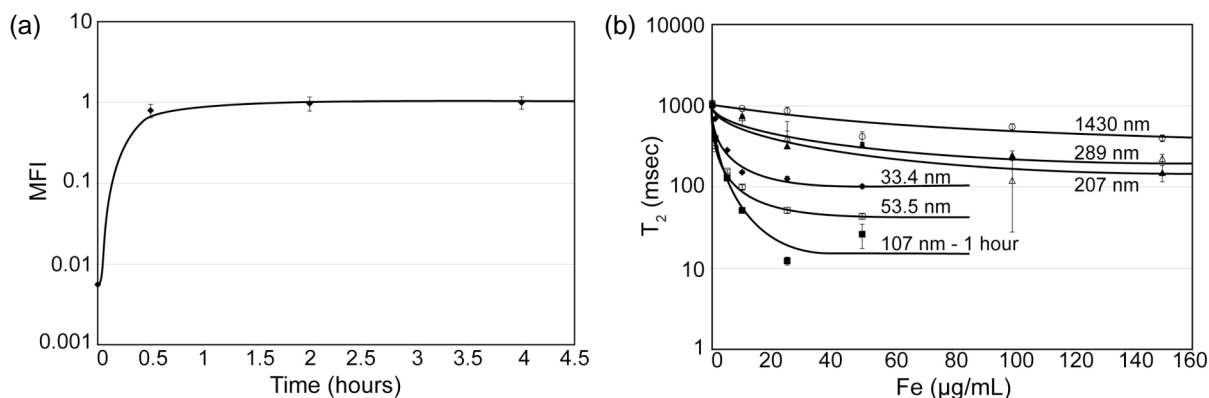


**Figure 6.** (a) Kinetics of NP uptake by living cells. NPs were labeled with the fluorescent dye FITC and uptake was quantified by flow cytometry. The mean fluorescence intensity (MFI) is plotted as a function of time. Data is shown for 107 nm NPs. (b) T<sub>2</sub> Relaxation times of cells labeled with NPs. Cells were labeled with NPs of various size and across a range of concentrations. The T<sub>2</sub> relaxivity of  $0.5 \times 10^6$  NP-loaded cells/mL in 300 µL was measured on a Bruker mq60 MR relaxometer operating at 1.41 T (60 MHz).

c. Image the localization of pNP-ONs in the cell cytoplasm (Months 18 - 24)

NP-ON conjugates were labeled with the fluorescent dye Cy5 so that intracellular localization could be observed by fluorescence microscopy. It was found that following a 4 hour incubation the NP-ON conjugates exhibited a punctate fluorescent pattern in the cytoplasm, indicative of endosomal/lysosomal entrapment (Figure 7). Lysosomal entrapment was confirmed through use of the lysosomal labeling dye, LysoTracker (Invitrogen).

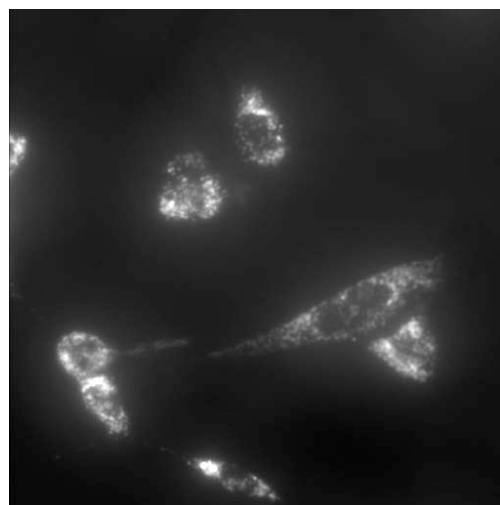


**Figure 7.** Intracellular localization of Cy5-labeled NP-ON conjugates.

d. Test various endosomal disruption agents to examine whether they can facilitate the delivery of pNP-ONs to the cytoplasm of cells (Months 24 - 30).

We have begun to test various endosomal disruption agents to improve the cytosolic delivery of NP-ON conjugates. Thus far we have tested chloroquine and tat-HA2 peptides. Unfortunately, neither of these agents led to a visible improvement in the delivery of the NPs to the cytosol. The NPs were still predominantly entrapped within lysosomes and exhibited similar fluorescent patterns as that shown in Figure 7. We have recently ordered several additional peptides and polymers to test, including GALA-INF3, INF7, and polypropyl acrylic acid. We also plan to test adenovirus as a means to encourage endosomal disruption.

### **Task 3. To detect c-myc expression in breast cancer cells (Months 30-33)**

- a. Incubate NP-ON conjugates with cell lysate from MCF-7, SK-BR-3, BT-20, and MDA-MB-231 breast cancer cells and take relaxation measurements before and after UV-exposure. Single NP-ONs will be used as a negative control (i.e. NP-ONs with only a single c-myc binding domain) (Months 30 - 33).

These studies have not yet commenced.

- b. Perform qRT-PCR of c-myc RNA isolated from each breast cancer cell line (Months 30 – 33)

We have determined that MCF-7 cells express ~8,000 copies of c-myc RNA/cell. We have not yet conducted qRT-PCR on the other cell lines listed in task 3a.

- c. Deliver pNP-ON into each breast cancer cell line and take relaxation measurements before and after UV exposure. Single pNP-ONs will be used as a negative control (Months 33 – 36).

These studies have not yet commenced.

### **KEY RESEARCH ACCOMPLISHMENTS:**

- Synthesized dextran-coated iron oxide NPs with hydrodynamic diameters ranging from ~20 nm to ~120 nm
- Synthesized aminated and carboxylated NPs
- Synthesized NPs with R2 relaxation times as high as 381 mM<sup>-1</sup>s<sup>-1</sup>
- Synthesized relatively monodisperse iron oxide NPs via thermal decomposition.
- Prepared gold-coated iron oxide NPs.
- Developed a click chemistry protocol (i.e. Cu-catalyzed terminal alkyne-azide cycloaddition) that resulted in NP-ON coupling efficiencies as high as 50%.
- Hybridization of 107 nm NP-ON conjugates to complementary DNA targets produced as much as a 61% change in T2 signal
- Detected as little as 10 pmoles of target
- Demonstrated that aminated NPs < 200 nm in diameter could be efficiently internalized into cells in less than 1 hr.
- Determined that NPs ~100 nm in diameter seem to be optimal for RNA detection in live cells.
- Confirmed cellular uptake of NP-ON conjugates by fluorescence microscopy.
- Determined that MCF-7 cells express ~8,000 copies of c-myc RNA/cell.

### **REPORTABLE OUTCOMES**

#### **Manuscripts:**

Thorek, D.L.J., **Tsourkas, A.** (2008) Size, charge, and concentration dependent uptake of iron oxide nanoparticles by non-phagocytic cells: a comparative study of USPIO, SSPIO, and MPIO. *Biomaterials*, 29(26): 3583-3590.

Thorek, D.L.J., Elias, D.R., **Tsourkas, A.** (2009) Comparative analysis of nanoparticle-antibody conjugations: carbodiimide versus click chemistry. Submitted.

#### **Podium Presentations:**

**Tsourkas, A.** (2009) Delineating molecular signatures of disease with novel molecular imaging probes. Biomedical Engineering Seminar Series, Department of Electrical and Computer Engineering, University of Delaware, Newark, DE.

**Tsourkas, A.** (2009) Delineating molecular signatures of disease with novel molecular imaging probes. Department of Biomedical Engineering Seminar Series, Carnegie Mellon University, Pittsburgh, PA.

**Tsourkas, A.** (2009) Delineating molecular signatures of disease with novel molecular imaging probes. Distinguished Speakers in Bioengineering Lecture, University of Toronto, Toronto, Ontario, Canada.

**Tsourkas, A.** (2008) Delineating molecular signatures of disease with novel molecular imaging probes. Department of Biomedical Engineering Seminar Series, Case Western Reserve University, Cleveland, OH.

**Tsourkas, A.** (2008) Magnetic nanoparticle-based detection of RNA transcripts. Department of Defense, Breast Cancer Research Program, Era of Hope Meeting, Baltimore, MD.

**Tsourkas, A.** (2008) *Molecular imaging: from drug development to the early detection of disease.* Department of Biomedical Engineering 10<sup>th</sup> Anniversary Symposium, Georgia Institute of Technology, Atlanta, GA.

**Tsourkas, A.** (2007) *Delineating molecular signatures of disease with novel molecular imaging probes.* Department of Biomedical Engineering Seminar Series, Rutgers University, Piscataway, NJ.

#### **Poster Presentations:**

Kimmel, J., Solomon, D., Hoang, D., **Tsourkas, A.** (2008) RNA detection using a magnetic relaxation switch. Biomedical Engineering Society, St. Louis, MO.

Thorek, L.J., Kimmel, J., Solomon, D., Hoang, D., Lee, H., **Tsourkas, A.** (2008) Magnetic nanoparticle-based detection of RNA transcripts. Department of Defense, Breast Cancer Research Program, Era of Hope Meeting, Baltimore, MD.

Thorek, D., **Tsourkas, A.** (2007) *Magnetic relaxation switch detection of cellular mRNA.* Biomedical Engineering Society, Los Angeles, CA.

#### **Undergraduates Supported by this Award:**

Christine Wang, B.S. Bioengineering, expected 2010. She will be supported Summer 2009.

Andrew Shenoy, B.S. Bioengineering, expected 2012. He will be supported Summer 2009.

Joseph Kimmel, B.S. in Bioengineering, 2008. Currently attending Mt. Sinai Medical School.

## **CONCLUSION:**

In summary, we have shown that we can synthesize dextran-coated superparamagnetic iron oxide nanoparticles with hydrodynamic diameters ranging from 20 nm to 120 nm. We have also shown that we can synthesize monodisperse NPs via thermal decomposition and that we can coat these NPs with gold.

We found that the 107 nm NPs can be used to detect as low as 10 pmoles of nucleic acid targets. Further, these NPs can be rapidly internalized into cells and exhibit higher contrast than the other NPs tested. Therefore, we will focus on NPs of this size when testing our RNA detection scheme in live cells.

Currently, it appears that our biggest obstacle will be limiting the extent of NP-ON entrapment within lysosomes. We plan to test a wide range of endosomal disruption agents in attempt to maximize the percent of NPs that make it to the cytosol.

## **REFERENCES:**

- 1) Thorek, D.L.J., **Tsourkas, A.** (2008) Size, charge, and concentration dependent uptake of iron oxide nanoparticles by non-phagocytic cells: a comparative study of USPIO, SSPIO, and MPIO. *Biomaterials*, 29(26): 3583-3590.
- 2) Park, J., An, K., Hwang, Y., Park, J., Noh, H., Kim, J., Park, J., Hwang, N., Hyeon, T. (2004) Ultra-large-scale syntheses of monodisperse nanocrystals. *Nature Materials*, 3, 891-895.
- 3) Thorek, D.L.J., Elias, D.R., **Tsourkas, A.** (2009) Comparative analysis of nanoparticle-antibody conjugations: carbodiimide versus click chemistry. Submitted.

## **APPENDICES:**

- 1) Thorek, D.L.J., **Tsourkas, A.** (2008) Size, charge, and concentration dependent uptake of iron oxide nanoparticles by non-phagocytic cells: a comparative study of USPIO, SSPIO, and MPIO. *Biomaterials*, 29(26): 3583-3590.
- 2) Thorek, D.L.J., Elias, D.R., **Tsourkas, A.** (2009) Comparative analysis of nanoparticle-antibody conjugations: carbodiimide versus click chemistry. Submitted.



Contents lists available at ScienceDirect

## Biomaterials

journal homepage: [www.elsevier.com/locate/biomaterials](http://www.elsevier.com/locate/biomaterials)

# Size, charge and concentration dependent uptake of iron oxide particles by non-phagocytic cells

Daniel L.J. Thorek, Andrew Tsourkas\*

Department of Bioengineering, University of Pennsylvania, 210 South 33rd Street, 240 Skirkanich Hall, Philadelphia, PA 19104, USA

## ARTICLE INFO

## Article history:

Received 25 March 2008

Accepted 16 May 2008

Available online xxx

## Keywords:

Molecular imaging

MRI

Ultrasmall superparamagnetic iron oxide

Standard superparamagnetic iron oxide

Micron-sized paramagnetic iron oxide

Nanoparticles

## ABSTRACT

A promising new direction for contrast-enhanced magnetic resonance (MR) imaging involves tracking the migration and biodistribution of superparamagnetic iron oxide (SPIO)-labeled cells in vivo. Despite the large number of cell labeling studies that have been performed with SPIO particles of differing size and surface charge, it remains unclear which SPIO configuration provides optimal contrast in non-phagocytic cells. This is largely because contradictory findings have stemmed from the variability and imprecise control over surface charge, the general need and complexity of transfection and/or targeting agents, and the limited number of particle configurations examined in any given study. In the present study, we systematically evaluated the cellular uptake of SPIO in non-phagocytic T cells over a continuum of particle sizes ranging from 33 nm to nearly 1.5  $\mu\text{m}$ , with precisely controlled surface properties, and without the need for transfection agents. SPIO labeling of T cells was analyzed by flow cytometry and contrast enhancement was determined by relaxometry. SPIO uptake was dose-dependent and exhibited sigmoidal charge dependence, which was shown to saturate at different levels of functionalization. Efficient labeling of cells was observed for particles up to 300 nm, however, micron-sized particle uptake was limited. Our results show that an unconventional highly cationic particle configuration at 107 nm maximized MR contrast of T cells, outperforming the widely utilized USPIO (<50 nm).

© 2008 Elsevier Ltd. All rights reserved.

## 1. Introduction

Continuing advancements in cell-based therapies have recently led to the emergence of cellular imaging as a strategy to track the migration and biodistribution of target cells in living organisms. Pre-clinical studies have already shown that cellular imaging can be used to evaluate stem cell distribution and homing in cell-based regenerative therapies [1,2]. Recently, cellular imaging has also allowed for improved assessment of functional efficacy and applicability of immunotherapeutic treatments in disease models for cancer [3–5] and AIDS [6].

In addition to evaluating cell-based therapies, cellular imaging also promises to provide a great deal of insight into diverse physiological and pathological phenomena. Interesting applications include the observation of monocyte recruitment to atherosclerotic lesions for the mapping of disease development and therapeutic intervention [7], imaging embryonic stem cell movement during embryonic [8] and organ development [9] and monitoring the dynamics of metastatic cellular extravasation and tissue invasion [10,11].

Tracking of labeled cells has been accomplished with a variety of imaging modalities including optical methods, positron emission

tomography (PET), single photon emission computed tomography (SPECT), and magnetic resonance (MR) imaging [12–14]. MR imaging presents a particularly promising approach because of its high spatial resolution in three dimensions and exquisite soft tissue contrast, which can be acquired concomitantly with the contrast-enhanced cellular distribution. MR detection of cells in vivo is often accomplished following labeling with superparamagnetic iron oxide (SPIO) particles. SPIO are negative contrast agents that are typically composed of an iron oxide crystal core surrounded by a polymer or polysaccharide shell [15]. A variety of manifestations of SPIO have been used to track cells, which can be broadly categorized as (1) ultrasmall SPIO (USPIO) with an overall diameter of 30–50 nm [16], (2) standard SPIO (SSPIO) with a diameter of 50–150 nm and (3) micron-sized paramagnetic iron oxide (MPIO) having a diameter approaching or greater than 1  $\mu\text{m}$  [17].

To date, USPIO has perhaps been the most widely utilized SPIO configuration for cell labeling. Although they provide less contrast enhancement per particle compared with SSPIO and MPIO, large numbers of particles can be loaded into each cell [18,19]. As cationic surfaces have been shown to facilitate cellular internalization [20,21], USPIO is often modified with polycationic cell permeating peptides (CPPs) such as HIV transactivator (TAT) [22] or protamine [23]. Other transfection techniques, sometimes in concert with CPPs, are also used [24,25].

\* Corresponding author. Tel.: +1 (215)898 8167; fax: +1 (215)573 2071.

E-mail address: [atsourk@seas.upenn.edu](mailto:atsourk@seas.upenn.edu) (Andrew Tsourkas).

An exciting new direction for cell tracking involves labeling cells with MPIO [26]. The large iron oxide cores present in these particles provide enough contrast for single cells to be imaged by MR. However, work with such large particles generally confines application of iron oxide labeling to phenotypes such as macrophages [18], dendritic cells [27] or hepatocytes that actively internalize foreign material. MPIO uptake in non-phagocytic cells has been accomplished, but is limited by the additional conjugation work and cost of using an antibody-mediated approach [28], which must be species specific and may induce adverse cellular events.

Recently, several studies have attempted to define an optimized particle configuration for iron oxide labeling of both phagocytic and non-phagocytic cell types. Although MPIO was excluded from all of these studies, it was found that phagocytic monocytes are more effectively labeled with SSPIO (150 nm) compared with USPIO (30 nm) [18,29]. Further, it was found that ionic carboxydextran-coated SSPIO (i.e. ferucarbotran) performed better than non-ionic dextran-coated SSPIO (i.e. ferumoxide) [18]. It remains unclear how MPIO compares with these agents; however, single cell detection has been achieved in phagocytic cells with both SPIO configurations [30,31].

The optimal SPIO configuration for labeling non-phagocytic cells has been much more elusive and findings have been contradictory. For example, in one study it was found that the delivery of carboxydextran USPIO and dextran-labeled SSPIO into non-phagocytic cancer cells and leukocytes (with the assistance of lipofection agents) was similar in terms of iron uptake [21]. Both particles led to higher iron uptake than USPIO. This indirectly suggests that larger particles with ionic coatings are superior to non-ionic USPIO. However, in a different study it was found that, in the presence of poly-L-lysine, ionic (aminated) USPIO exhibited significantly higher iron uptake in non-phagocytic cells compared with SSPIO. These data suggest that smaller ionic particles are internalized into non-phagocytic cells more efficiently [32]. These contradictory findings likely stem from the variability and imprecise control over surface charge and the limited number of particle configurations examined, particularly with respect to diameter (ranging only from ~17 nm to 150 nm).

In the present study we systematically evaluated the cellular uptake of SPIO in non-phagocytic T cells over a continuum of particle sizes ranging from 33 nm to nearly 1.5  $\mu\text{m}$  and with precisely controlled surface properties. T cells were selected as a model non-phagocytic phenotype since visualization of their distribution is expected to be of importance for adoptive T cell therapy for cancer and T cell homing in autoimmune diseases. Extremely fine control was exerted on the surface properties of SPIO by direct chemical modification of particle surfaces rather than attempting to modulate the density of supplemental transfection agents. Concentration effects and incubation times were also tested in the interest of isolating the role particle size exerts on individual cell uptake and overall contrast enhancement. Our work shows that in a space between USPIO and MPIO exist configurations of relatively small particles (~100 nm) that efficiently label non-adherent, non-phagocytic T cells and generate higher relaxivity (per cell) relative to particles of other sizes.

## 2. Materials and methods

### 2.1. Nanoparticle synthesis

Three different formulations of dextran-coated superparamagnetic iron oxide nanoparticles were prepared using the co-precipitation method [33]. All three formulations were prepared following the same procedure, as described below, with the only difference being the amount of  $\text{FeCl}_2$  and  $\text{FeCl}_3$  added. Specifically, 25 g of dextran T10 (GE Healthcare, Piscataway, NJ) was dissolved in 50 mL of  $\text{dH}_2\text{O}$  and heated to 80 °C for 1 h. The solution was allowed to return to room temperature and continued to mix overnight. Subsequently, the dextran was cooled to 4 °C on ice and degassed with  $\text{N}_2$  for 1 h.  $\text{FeCl}_2$  (0.7313 g, 1.5 g, or 2.2 g) and  $\text{FeCl}_3$  (1.97 g, 4 g, or

6 g, respectively) were each rapidly dissolved in 12.5 mL of degassed  $\text{dH}_2\text{O}$  and kept on ice for approximately 10 min. The iron solutions were added to the dextran simultaneously and allowed to mix for 30 min. Keeping this mixing solution at 4 °C, 15 mL of ammonium hydroxide was added. The resulting black viscous solution was then heated to 90 °C for 1 h then cooled overnight, followed by ultracentrifugation at 20 krcf for 30 min. Pellets were discarded and the supernatant was continually diafiltered using a 100-kDa MWCO cartridge (GE Healthcare) on a peristaltic pump (E323, Watson Marlow Bredel, Wilmington, MA). The particles were exchanged into 0.02 M citrate, 0.15 M sodium chloride buffer until all unreacted products had been removed. Aminated silica-coated iron oxide micro-particles were purchased from Bioclone Inc. (San Diego, CA). Amine functionalized styrene copolymer-coated iron oxide particles (Adembeads) were purchased from Ademtech SA (Pessac, France).

### 2.2. Amination of particles

Amination and crosslinking of the coating on the dextran-SPIO were accomplished through reaction of the SPIO with 25% 10 M NaOH and 33% epichlorohydrin [34]. After mixing for 24 h, additional ammonium hydroxide was added to the solution, bringing the volume fraction to 25% ammonium hydroxide, and the reaction was allowed to proceed for another 24 h. The particles were then exhaustively purified via diafiltration. The resulting particles were amine functionalized crosslinked iron oxide.

### 2.3. FITC labeling and amine-blocking of particles

All SPIO particles were labeled with FITC at a FITC-to-iron molar ratio of 19.2:1. FITC was reacted with particles for 4 h followed by two rounds of gel purification, once on a NAP-5 column and then on a PD10 column (GE Healthcare), both equilibrated with PBS. The FITC-labeled SPIO was subsequently reacted with various volumes of glycidol (0.01–50%) to produce populations of particles with different amine content. The particles were cleaned of excess glycidol through repeated precipitation in isopropanol and resuspension in PBS. Amine-blocking was also attempted with particles of 200 nm and greater, but this modification impelled immediate particle insolubility.

### 2.4. Measurement of particle size

The hydrodynamic diameter of the dextran-coated and commercial iron oxide particles was measured using a Zetasizer Nano-z (Malvern Instruments, Malvern, UK) through dynamic light scattering (DLS). The dextran-coated SPIO particles were diluted in PBS to a concentration of approximately 0.5 mg/mL and read in triplicate. The commercial particle diameters were read in the same manner, but only after undergoing three washes by precipitation in the presence of a strong magnet and resuspension in PBS. The values reported for all samples are the intensity peak values.

### 2.5. Measurement of particle cores

Transmission electron micrographs of all iron oxide particles were taken using a JEOL 2010 at 200 kV. Samples were prepared for imaging by evaporating the particles onto a carbon-coated copper grid (Holey carbon – mesh 200, Structure Probe Inc., West Chester, PA). Salt was removed from all of the samples prior to evaporation by exchanging the particles into  $\text{dH}_2\text{O}$ . Images of particle cores were analyzed using ImageJ (National Institutes of Health, Bethesda, MD). Since many of the particles were found to be composed of a cluster of multiple iron oxide cores, the average diameter of each core and the average number of cores per particle were determined. Assuming each core to be spherical, the amount of iron per particle type was determined from the aggregate core volume.

### 2.6. Measurement of particle relaxivity ( $R_1$ and $R_2$ )

The longitudinal ( $R_1$ ) and transverse ( $R_2$ ) relaxivity of each particle was calculated as the slope of the curves  $1/T_1$  and  $1/T_2$  against iron concentration, respectively.  $T_1$  and  $T_2$  relaxation times were determined using a Bruker mq60 MR relaxometer operating at 1.41 T (60 MHz).  $T_1$  measurements were performed by collecting 12 data points from 5.0 ms to 1000 ms with a total measurement duration of 1.49 min.  $T_2$  measurements were made using  $\tau = 1.5$  ms and two dummy echoes, and fitted assuming monoexponential decay.

### 2.7. Measurement of number of amines per particle

The number of amines per particle was determined following the general procedure described by Zhao et al. [35]. Briefly, iron oxide particles at a concentration of 2 mg/mL Fe were reacted with excess *N*-succinimidyl 3-(2-pyridyldithio) propionate (SPDP, Calbiochem, San Diego, CA) for 4 h. SPIO was washed of excess SPDP through repeated precipitation in isopropanol and resuspension in PBS. The particles were then run through a 50-kDa MWCO centrifugal filter (YM-50, Millipore, Billerica, MA) either with or without the addition of disulfide cleavage agent TCEP. The difference of the absorbance of these two samples at 343 nm was used to determine the



concentration of SPDP in the filter flow. Adjusting for dilution, the number of amines per particle was determined.

## 2.8. Cell culture and labeling

Immortalized human T cells, Jurkat Clone E6-1 (ATCC), were maintained at 37 °C in 5% CO<sub>2</sub> in RPMI 1640 (Mediatech, Manassas, VA) media supplemented with 10% FBS (Hyclone, Logan, UT) and penicillin/streptomycin (Mediatech). T cells were labeled with iron oxide particles by incubating the commercial and lab-made particles with  $2 \times 10^6$  cells in 400  $\mu$ L of fully supplemented media for 1 h or 4 h, at 37 °C in 5% CO<sub>2</sub>. Cells were washed of non-internalized particles through two methods. Synthesized dextran-coated particles were washed from cells using centrifugation. Specifically, cells were pelleted at 0.5 rcf for 5 min and resuspended in PBS. This was repeated three times. The dextran-coated particles are highly soluble in aqueous solvents and do not precipitate at these centrifugation speeds. Removal of non-internalized commercial particles was accomplished through a density gradient. The cells and particles were diluted to 1 mL with PBS and overlaid on 4 mL of room temperature Ficoll-Paque PLUS (GE Healthcare). The sample was centrifuged at 0.4 rcf for 40 min. Cells loaded with particles were retrieved from the interface layer. To determine if particles were internalized or merely adsorbed on the cell exterior, surface receptor cleavage enzyme trypsin was used. Following particle incubation, as described above, cells were exposed to 0.025% trypsin-EDTA (Invitrogen) for 5 min. Purification of non-internalized particles was carried out as detailed. No statistical difference was seen in either flow cytometry or relaxometry between groups washed with or without enzyme.

## 2.9. Flow cytometry and relaxation measurements

Immediately after non-internalized iron oxide particles were removed from T cell samples, flow cytometry was performed on a Guava Easycyte (Guava Technologies, Hayward, CA). For labeling and viability experiments, forward and side scatterings were used to identify the entire population of cells. Data analysis of flow cytometry data was accomplished with FlowJo (TreeStar, Ashland, OR). Viability of T cells was determined using the LIVE/DEAD cytotoxicity kit for mammalian cells (Invitrogen, Carlsbad, CA) according to the manufacturer's instructions. In order to evaluate the decrease in  $T_2$  relaxation time of iron oxide internalized T cells, purified cells were lysed for 30 min in 0.1% SDS in PBS at 37 °C. Samples were diluted to  $0.5 \times 10^6$  cells/mL in 300  $\mu$ L and  $T_2$  relaxation times were measured using the benchtop relaxometer. All flow and magnetic resonance measurements were made in triplicate on at least two separate occasions.

# 3. Results and discussion

## 3.1. Particle synthesis and characterization

Three different formulations of dextran-coated superparamagnetic iron oxide nanoparticles were prepared via co-precipitation. All three syntheses utilized a ratio of approximately three ferrous to ferric iron chloride; however, the total amount of iron was increased by whole numbers, i.e.  $2 \times$  and  $3 \times$  irons, respectively. This deviation in the amount of iron present during synthesis allowed for the manufacture of SPIO with a range of different sizes and properties. Specifically, DLS of the SPIO, following crosslinking and amination of the dextran coating, indicated average hydrodynamic radii of 33.4 nm, 53.5 nm and 107 nm, respectively, with the larger nanoparticles corresponding to syntheses that utilized more iron. When the total amount of iron was increased further, the co-precipitation solution became extremely viscous and yielded highly dispersed aggregates that precipitated out of solution. Therefore, nanoparticles ranging from 200 nm to 1  $\mu$ m in diameter were acquired from commercial sources. Specifically, superparamagnetic iron oxide particles of 200 nm and 300 nm diameter with an amine functionalized styrene copolymer coating (Amino-Ademabeads) were purchased from Ademtech, while amine functionalized silica-coated 1  $\mu$ m diameter particles were purchased from Bioclone. This allowed particle sizes across nearly three orders of magnitude to be compared.

The particle sizes as determined by DLS, peak intensity values, are compared in Fig. 1. The 33.4 nm, 53.5 nm and 107 nm dextran-coated SPIO samples were fully soluble at physiological conditions. Conversely, it was found that the large size of the 289 nm and 1430 nm particles led to rapid precipitation. Settling was also

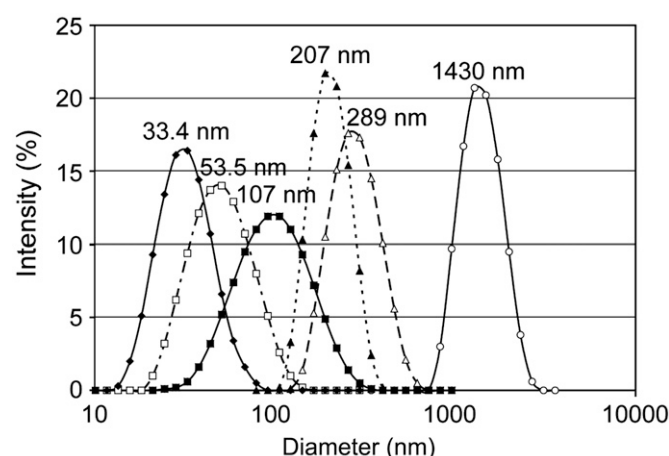


**Fig. 1.** Hydrodynamic diameter of SPIO. The hydrodynamic diameter of SPIO particles was determined by DLS. Intensity measurements are reported and the peak intensity is provided for each distribution.

a concern for the 207 nm particles; however, full precipitation generally took several hours.

Analysis of the iron oxide core size and structure of the magnetic particles was conducted using TEM. Representative micrographs are shown in Fig. 2. Aggregation of particles in salt free solution was a problem during TEM sample preparation; however, reduction in sample concentration allowed for imaging of discretely distributed particles. Iron cores were easily distinguished from carbon-coated copper grids, while dextran and styrene copolymer were not visible because of their low electron density.

An interesting feature of the dextran-coated nanoparticles is that each particle consists of a cluster of one or more iron oxide cores, with each core being approximately equal in size. Specifically, the distribution of cores is centered at approximately 6 nm for all three dextran-coated nanoparticles (Fig. 3); however, the average number of cores per particle increases with overall hydrodynamic diameter. In contrast, the larger 207 nm and 289 nm styrene copolymer-coated particles exhibited a single large spherical iron oxide core, while the 1.43  $\mu$ m silica-coated particles exhibited an amorphous iron oxide core of no discrete size or shape. A summary of the properties of each SPIO is provided in Table 1.

The  $R_1$  and  $R_2$  data (Figs. 4 and 5), also summarized in Table 1, indicate that there is a trend of increasing  $R_2$  and decreasing  $R_1$  with size up to the 107 nm particles. For particles of greater size, the single large core of the 207 nm and 289 nm particles does not translate into proportionately higher  $R_2$ . This likely reflects lower crystallinity of the larger single iron oxide cores in comparison to smaller crystals [36]. Furthermore, according to the Solomon-Bloembergen theory, which relates the relaxation rate to particle properties, the total size of the particle is not critical to the magnitude of  $R_2$  as the susceptibility effect falls off from the surface with an exponential ( $r^6$ ) dependence [37,38]. It should be noted that the  $R_1$  values reported for particles greater than 200 nm are likely underestimates due to precipitation of the particles during  $T_1$  measurements. For instance, determining  $T_1$  relaxation times required more than 100 s per sample, which was an ample time for the micrometer-sized particles to precipitate out of solution.

## 3.2. Cell loading

The extent to which T cells internalize iron oxide particles is not only dependent on particle size but also various other particle characteristics and cell loading conditions, including surface charge, particle concentration, and incubation time. Thus, before it

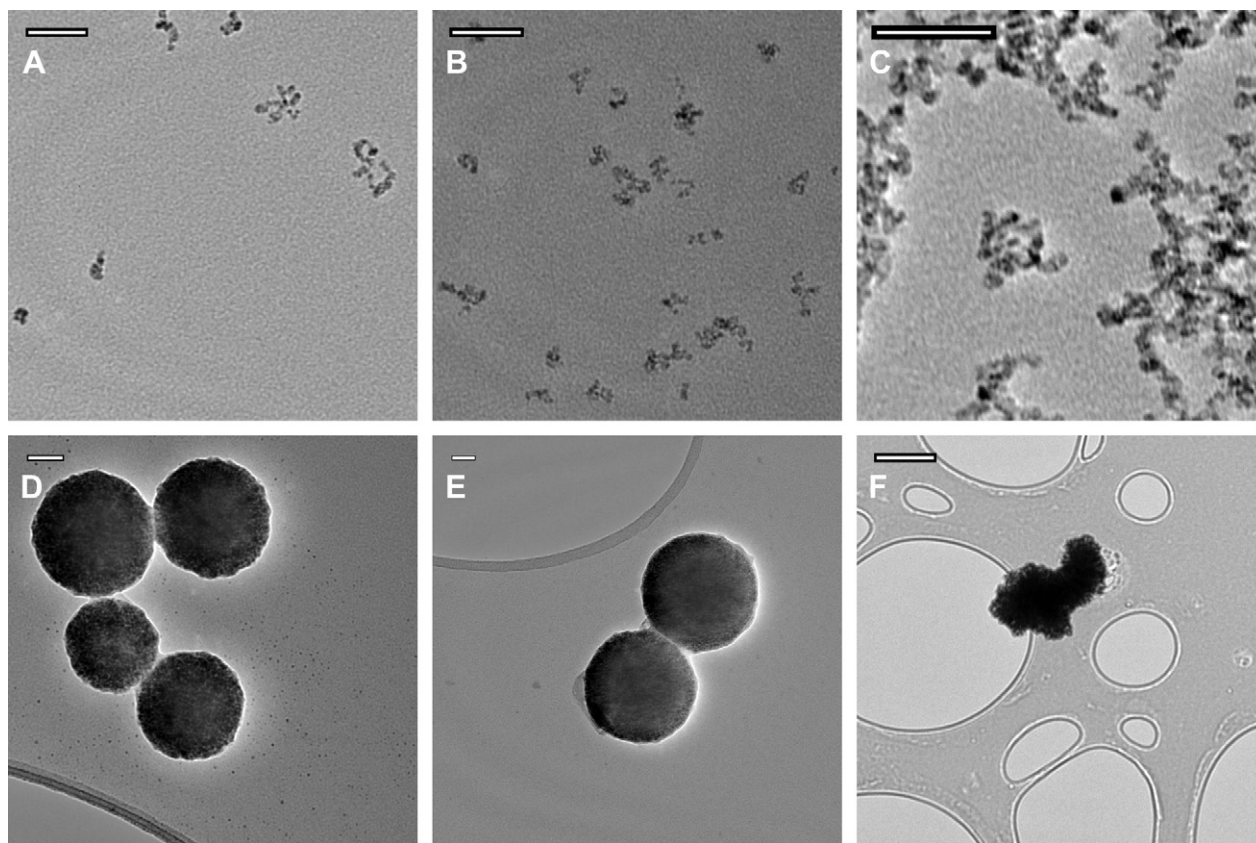


**Fig. 2.** TEM of SPIO cores. High magnification transmission electron microscopy images of the iron oxide particles were obtained with a JEOL 2010 operating at 200 kV. Structure analysis revealed the multiple core nature of the (A) 33.4 nm, (B) 53.5 nm and (C) 107 nm dextran-coated SPIO. Larger particles were composed of single cores; (D) 207 nm, (E) 289 nm and (F) 1430 nm. All scale bars are 50 nm, excluding (F) 1  $\mu$ m.

could be determined which particle size led to the highest relaxivity per cell, it was first necessary to identify conditions whereby cell loading was independent of these other parameters. The use of fluorescently labeled iron oxide particles combined with flow cytometry provided a facile method by which particle uptake could be systematically assessed in a high-throughput manner. In the current study, all SPIO samples were fluorescently labeled with an equivalent amount of FITC/iron.

### 3.2.1. Concentration

In order to confirm that iron oxide particles were present in sufficient quantity for maximum cellular uptake, T cells were incubated with increasing iron concentrations until a saturating level was reached. As shown in Fig. 6, dextran-coated particles were efficiently internalized, all reaching a plateau at iron concentrations below 50  $\mu$ g/mL. Greater than 100  $\mu$ g/mL was required to saturate the loading of the 207 nm, 289 nm and 1430 nm particles. The necessity for these higher iron concentrations may be attributed to the fact that the number of particles per unit of iron is far less than the smaller agents. Further, there is likely less contact between the larger particles and the suspended cells because of their continual sedimentation. This was perhaps most evident with MPIO, where cell labeling was poor across all particle concentrations. Even at 1000  $\mu$ g/mL (data not shown) labeling with MPIO did not reach the levels achieved by the dextran-coated USPIO and SPIO.

### 3.2.2. Surface properties

Surface charge is important for intracellular delivery of exogenous material. This principle has been described for a variety of nanoparticle (examples include gold [39], polymer [40,41] and silica [42]) and biological (for example, delivery of DNA with

cationic proteins, lipids and polymers [43]) contexts. The aminated surfaces of the particles used in this study provide an inherent surface charge, facilitating cellular interaction. However, in order to study the role this property has in the intracellular delivery of iron oxide contrast agent, it is necessary to manipulate the magnitude of the surface charge. To do so we have applied glycidol, a hydroxyl terminating epoxide, to generate subsets of particles with a gradient of surface amines. Glycidol has been used previously in dendrimer chemistry to reduce the chemotoxicity of highly-positively charged dendrimers [44]. The tight control of surface properties produced by consuming amines with glycidol allows for isolated examination and evaluation of the role of surface charge on SPIO.

The summary of particle uptake on a per cell basis is shown in Fig. 7(A–C). Each data point represents the normalized mean fluorescence intensity (MFI) of T cells that were incubated with iron oxide particles at a saturating concentration (previously determined) for 4 h. Under these incubation conditions, it was found that particles in their natural (fully aminated) state are maximally internalized. Any further increase in the positive surface charge will not further augment SPIO loading. In other words, the efficiency of cell labeling has become independent of surface charge. In all cases, uptake and internalization of the particles were rapid. Representative uptake of the 107 nm particles as a function of time is shown in Fig. 7(D).

### 3.2.3. Viability

The impact and potential cytotoxicity of each iron oxide particle on T cells were measured using a two-color fluorescent cell viability kit. Negligible to low levels of cell death were observed (Fig. 8) for all particles at diminished and saturating concentrations of iron oxide (10  $\mu$ g/mL and 50  $\mu$ g/mL, respectively). The exception was for



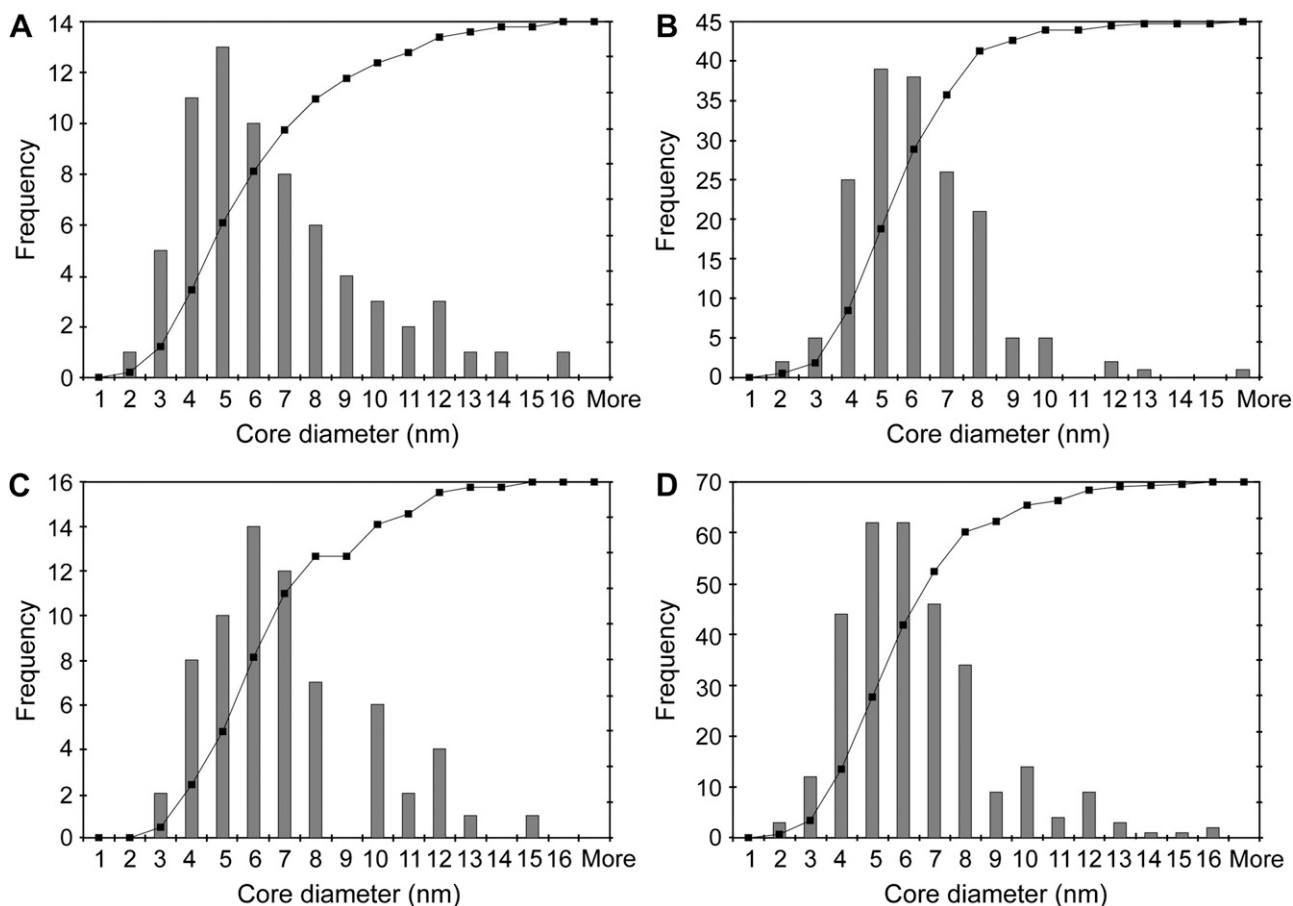


**Fig. 3.** Size distribution of SPIO core diameters. TEM measurements of the SPIO core diameter for (A) 33.4 nm, (B) 53.5 nm, (C) 107 nm and (D) all cores. The cores diameters were analyzed assuming that they were spherical and the frequency and cumulative distributions are plotted. Particle size appears to be determined by the number of cores per particle rather than the size of those constituent cores.

**Table 1**  
Physical and magnetic properties of SPIO

Hydrodynamic diameter (nm)	Core diameter (nm)	Number of cores	$R_2$ (/mm/s)	$R_1$ (/mm/s) <sup>a</sup>	$R_2/R_1$	NH <sub>2</sub> /particle	Fe (atoms)/particle <sup>b</sup>	Coating material
33	6.067	1.9	71.00	13.56	5.24	185	8924	Dextran
53	5.603	5.3	82.25	9.97	8.25	631	20,065	Dextran
107	6.534	11.2	381.00	7.24	52.66	1024	66,729	Dextran
207	175.4	1	176.58	0.51	344.48	$6.0 \times 10^5$	$6.3 \times 10^7$	Styrene copolymer
289	289.6	1	115.20	0.34	337.43	$2.2 \times 10^6$	$2.6 \times 10^8$	Styrene copolymer
1430	–	1	64.32	0.41	156.49	$8.5 \times 10^8$	$1.3 \times 10^7$	Silica

<sup>a</sup>  $R_1$  values for 207 nm, 289 nm and 1430 nm particles may be underestimated due to precipitation during measurements.

<sup>b</sup> Measurement of Fe (atoms)/particle for the commercial particles was made using the company provided relative iron mass per particle data, rather than the core size determination from TEM.

the 107 nm SPIO, which exhibited some adverse cell influence even at 10  $\mu$ g/mL. This effect was exacerbated at increased concentrations. When the amines on the 107 nm particle were completely blocked, cell death was reduced to negligible levels; however, internalization was also reduced to negligible levels (Fig. 7C). T cell death is likely attributable to the high positive surface charge possessed by the SPIO. Similar results have been seen with amine-terminated poly(amidoamine) dendrimers [45]. The extremely high driving force for cell internalization imparted by positive SPIO surface charge can lead to cell death.

In order to minimize the toxicity of the 107 nm particles, the incubation time with T cells was decreased to 1 h. As shown in Fig. 7D, particle uptake is still saturated within this time frame, therefore exposing T cells to excess SPIO for longer periods of time was deemed unnecessary. No toxicity was observed with the 107 nm particles after just 1 h of incubation.

### 3.2.4. Magnetic contrast enhancement

Flow cytometry was utilized to determine the saturating conditions for each SPIO; however, these single cell measurements were conducted with some variation between the number of fluorescent labels per particle making it difficult to accurately quantify the number of particles per cell. Also, after labeling cells with superparamagnetic tracking agents the critical assessment of ability to track cells is their relaxivity. Therefore, a benchtop NMR minispectrometer, near the clinical field strength of 1.5 T, was utilized for evaluating in vitro loading. As shown in Fig. 9, T cells loaded with particles showed a dose-dependent, negative contrast enhancement.

As befits their widespread application in the literature, the USPIO proved effective at lowering the spin–spin relaxation time ( $T_2$ ). Despite delivering only a small payload of iron per particle, the large numbers of 33.4 nm and 53.5 nm particles that accumulate in

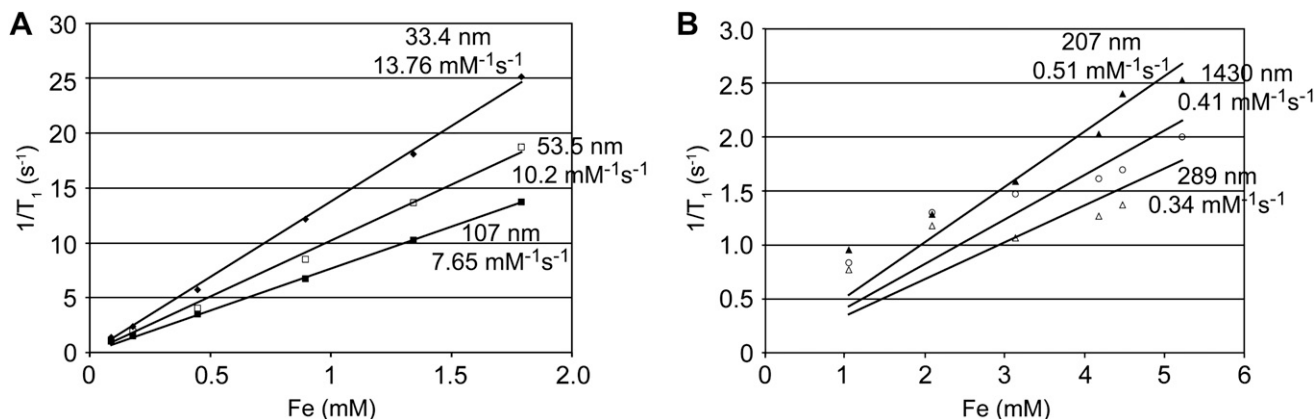


**Fig. 4.**  $T_1$  relaxivity ( $R_1$ ) measurements of SPIO. SPIO of various sizes were diluted in PBS to iron concentrations between (A) 0.1 mM and 2 mM or (B) 1 mM and 6 mM.  $T_1$  values were then obtained using the minimum time sequence required to get reproducible values, because of precipitation issues. The inverse of the  $T_1$  time, in seconds, was linearly fit against concentration to yield the particle  $R_1$ .

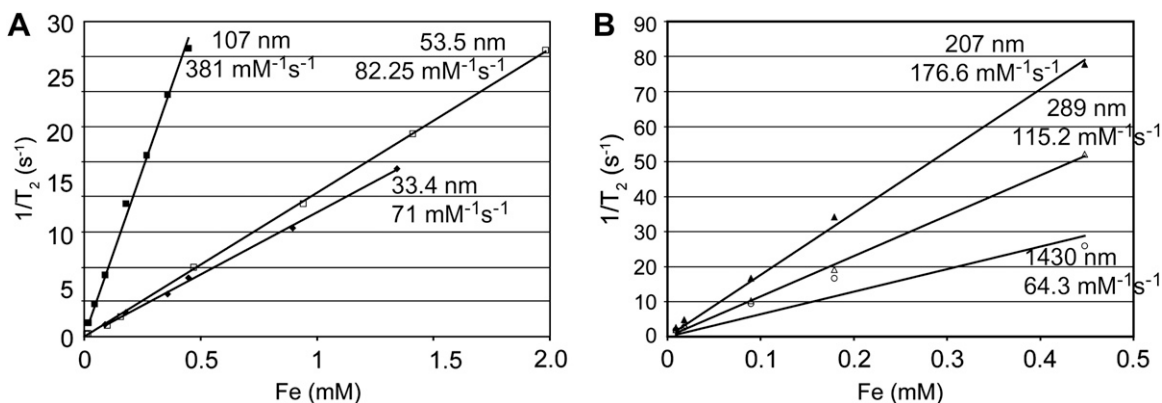


**Fig. 5.**  $T_2$  relaxivity ( $R_2$ ) measurements of SPIO. SPIO of various sizes were diluted in PBS to iron concentrations between (A) 0.1 mM and 2 mM or (B) 0.01 mM and 0.5 mM. The  $T_2$  values were then obtained using a monoexponential curve fit. The inverse of these values, plotted against concentration, gives the  $R_2$ . Precipitation of the 1430 nm particles resulted in nonlinearity.

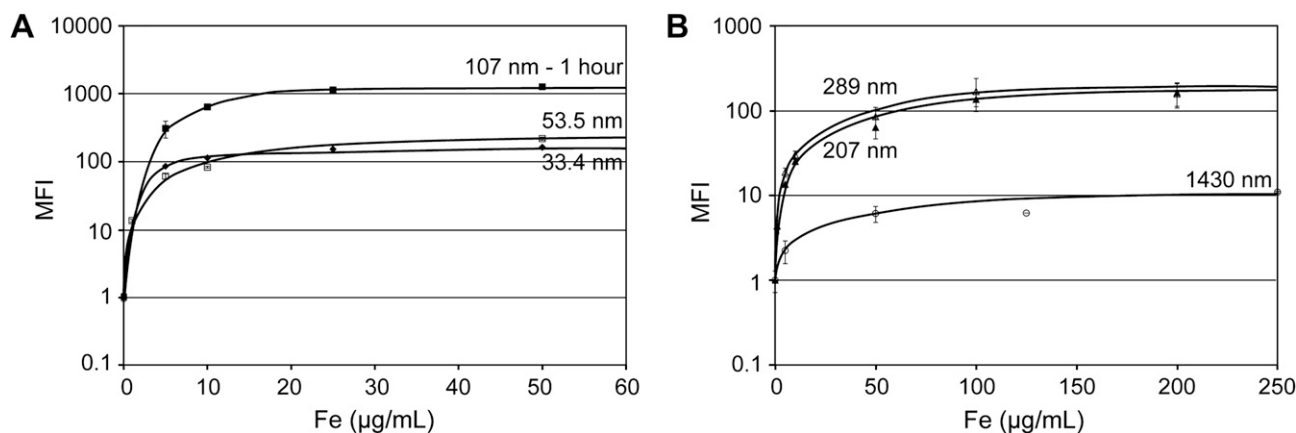


**Fig. 6.** Dependence of SPIO loading on particle concentration. Fluorescently labeled SPIO of various sizes and across a range of concentrations was incubated with  $2 \times 10^6$  T cells/mL at 37 °C for 4 h (excluding the 107 nm particle as indicated). SPIO uptake was then measured by flow cytometry. Each experiment was conducted in triplicate on at least two separate occasions and each data point represents the average value for the mean fluorescent intensity (MFI). Note the difference in x- and y-axes for (A) and (B).

the cells allow for a strong aggregate effect, producing an average  $T_2$  signal of 126.05 ms and 51.5 ms under saturating conditions, respectively. These reduced signal values correlate to an 8.04 and 19.68 times reduction in signal from T cells without any contrast agent ( $T_2 = 1013$  ms).

Performance of particles greater than 200 nm was ranked inversely with diameter. Greater concentrations of large particles

continued to reduce the  $T_2$  signal; however, when the iron concentration was increased above 500  $\mu\text{g/mL}$  the methods used to distinctly separate loaded-cells from free particles became less reliable. It should be noted that this drawback does not exist for the flow cytometry measurements, as the particles themselves could be excluded from the cells based on forward and side scatter. At 150  $\mu\text{g/mL}$  Fe, the spin-spin relaxation signal from the 207 nm,

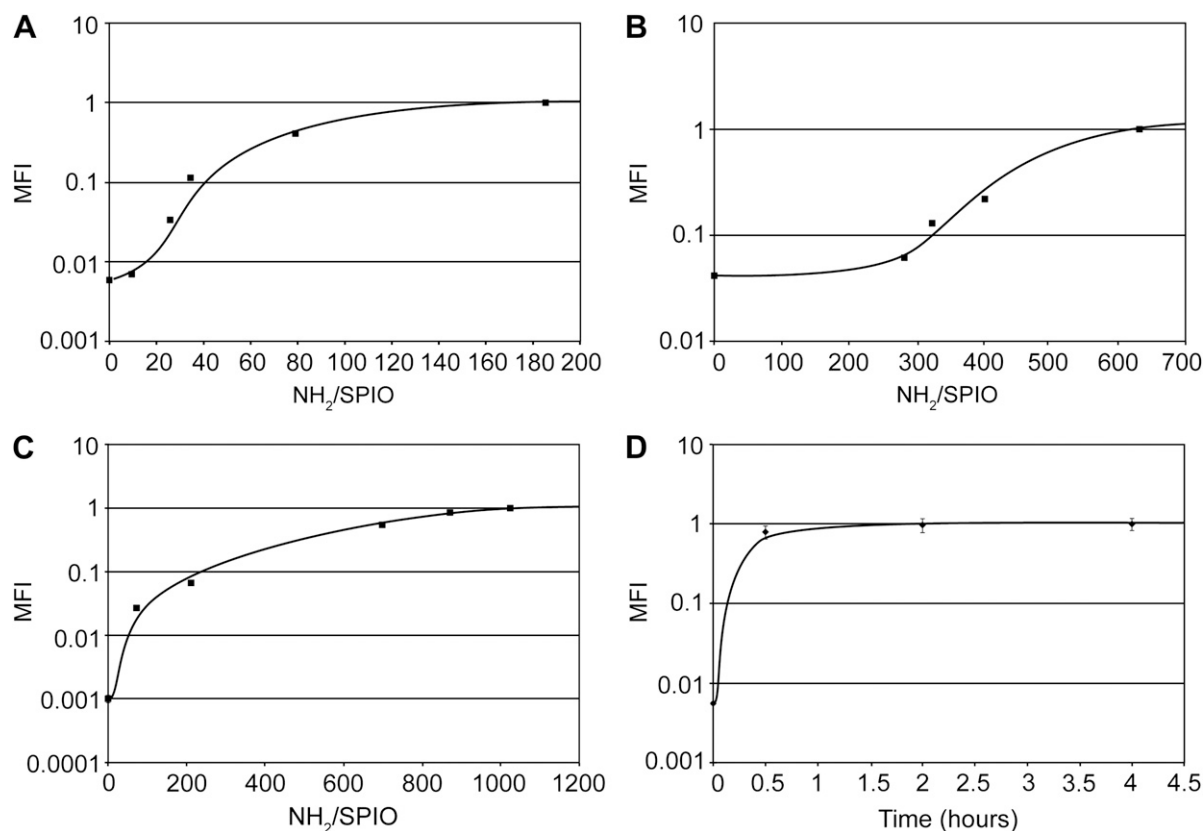


**Fig. 7.** Dependence of SPIO loading on surface charge. T cell uptake of fluorescently labeled SPIO as a function of surface charge was examined by modulating the number of amines per particle for the (A) 33.4 nm, (B) 53.5 nm and (C) 107 nm particles. A gradient in the degree of functionalization was produced by glycidol blocking of amines. SPIO was incubated with T cells at saturating concentrations, 50  $\mu\text{g}/\text{mL}$ , under identical conditions. Flow cytometry was then performed to assess the relative uptake of each SPIO. Each data point represents the mean fluorescent intensity (MFI). The loading of SPIO was rapid; Fig. 7(D) shows the representative uptake of fully-aminated 107 nm particles.

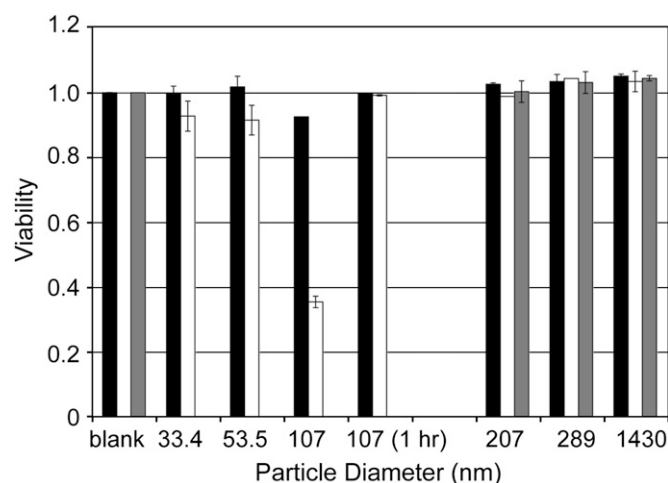


**Fig. 8.** Viability of T cells incubated with SPIO. SPIO was incubated with T cells at various iron concentrations: 10  $\mu\text{g}/\text{mL}$  [black], 50  $\mu\text{g}/\text{mL}$  [white] and 100  $\mu\text{g}/\text{mL}$  [grey]. After 4 h (unless otherwise noted), viability was measured and normalized to cells grown in the absence of any particles (blank). All SPIO exhibited negligible impact on cell survival after 4 h, excluding the 107 nm diameter particles. Reducing incubation time of these particles to 1 h eliminated adverse effects at both low and saturating concentrations.

289 nm and 1430 nm particles was 149.75 ms, 224.3 ms and 398 ms. These findings suggest that despite their high  $R_2$  values and large iron content, particles greater than 200 nm seem to have limited applicability in labeling non-phagocytic cells.

The highly-aminated SPIO with a diameter of 107 nm produced the greatest contrast enhancement. These particles combined the

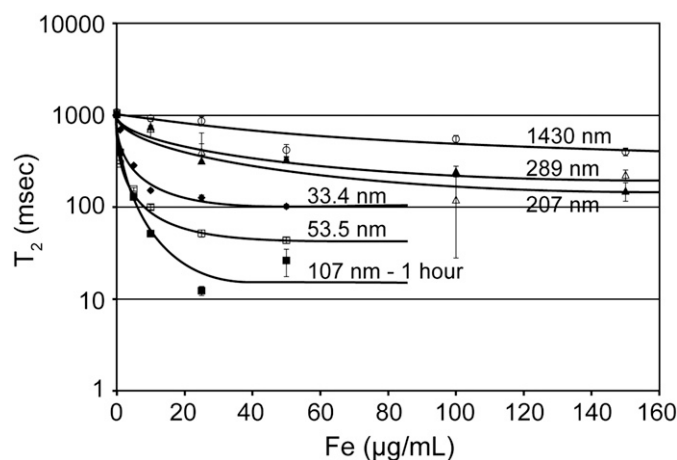


**Fig. 9.**  $T_2$  relaxation times of T cells labeled with SPIO. T cells were labeled with SPIO of various sizes and across a range of concentrations. The  $T_2$  relaxivity of  $0.5 \times 10^6$  SPIO-loaded T cells/mL in 300  $\mu\text{L}$  was measured on a Bruker mq60 MR relaxometer operating at 1.41 T (60 MHz). The signal decrease observed following internalization of SPIO is dose-dependent and saturation correlates well with values determined by flow cytometry. The 107 nm SSPIO produced maximum signal decrease.

high degree of internalization of the USPIO with the superior relaxivity of larger particles. At the 1 h loading time, to avoid any longer term cytotoxic events, these SSPIO were able to reduce signal approximately two orders of magnitude, providing  $T_2$  signal of only 12.25 ms, or an 82.74 times reduction in signal from control. This reduction in signal was approximately five and 10 times greater than that produced by the 53.5 nm and 33.4 nm SPIO (for the same concentration).

#### 4. Conclusions

In this work, efficient iron oxide labeling, without the use of cell penetrating peptides or transfection agents, was accomplished in a clinically relevant non-phagocytic cellular system. The level of SPIO loading in T cells was determined by flow cytometry and verified through evaluation of MR contrast enhancement. Using conditions under which cell loading was independent of particle concentration, chemical surface modification, and incubation time, particle size was isolated as an attribute to affect nano- and microparticle loading. Large particles, over 200 nm in diameter, possess much greater amounts of iron per particle, and thus theoretically require few particles or a single particle per cell in order to be used. However, they suffered from gravitational sedimentation, decreased efficiency of cell labeling, and in some cases free particles were incompletely removed from labeled cells. This may not be a problem with adherent and/or phagocytic cell systems, but significantly hampered their efficacy as magnetic labeling probes for non-phagocytic suspended cells. The vastly greater number of USPIO that accumulate within the cells made up for their weaker  $R_2$  values. While a general trend correlating increased or decreased particle size with labeling was not observed, it was clear that the 107 nm SPIO manifestation led to the largest  $T_2$  signal decrease.

#### Acknowledgments

D.L.J.T. was supported by NIH T32 HL007954-07, Multidisciplinary Training in Cardiovascular Biology. This work was supported in part by Wyeth Pharmaceuticals, the Transdisciplinary Program in Translational Medicine and Therapeutics, the Lupus Research Institute, and the DOD Breast Cancer Research Program of the Office of the Congressionally Directed Medical Research Programs (BC061856).

#### References

- [1] Bulte JW, Douglas T, Witwer B, Zhang SC, Strable E, Lewis BK, et al. Magnetodendrimers allow endosomal magnetic labeling and in vivo tracking of stem cells. *Nat Biotechnol* 2001;19(12):1141–7.
- [2] Rogers WJ, Meyer CH, Kramer CM. Technology insight: in vivo cell tracking by use of MRI. *Nat Clin Pract Cardiovasc Med* 2006;3(10):554–62.
- [3] Ahrens ET, Flores R, Xu HY, Morel PA. In vivo imaging platform for tracking immunotherapeutic cells. *Nat Biotechnol* 2005;23(8):983–7.
- [4] Pittet MJ, Grimm J, Berger CR, Tamura T, Wojtkiewicz G, Nahrendorf M, et al. In vivo imaging of T cell delivery to tumors after adoptive transfer therapy. *Proc Natl Acad Sci U S A* 2007;104(30):12457–61.
- [5] Sauer MG, Ericson ME, Weigel BJ, Herron MJ, Panoskaltis-Mortari A, Kren BT, et al. A novel system for simultaneous in vivo tracking and biological assessment of leukemia cells and ex vivo generated leukemia-reactive cytotoxic T cells. *Cancer Res* 2004;64(11):3914–21.
- [6] Sundstrom JB, Mao H, Santoianni R, Villinger F, Little DM, Huynh TT, et al. Magnetic resonance imaging of activated proliferating rhesus macaque T cells labeled with superparamagnetic monocrySTALLINE iron oxide nanoparticles. *J Acquir Immune Defic Syndr* 2004;35(1):9–21.
- [7] Kircher MF, Grimm J, Swirski FK, Libby P, Gerszten RE, Allport JR, et al. Non-invasive in vivo imaging of monocyte trafficking to atherosclerotic lesions. *Circulation* 2008;117(3):388–95.
- [8] Hadjantonakis AK, Papaioannou VE. Dynamic in vivo imaging and cell tracking using a histone fluorescent protein fusion in mice. *BMC Biotechnol* 2004;4.
- [9] Puri S, Hebrok M. Dynamics of embryonic pancreas development using real-time imaging. *Dev Biol* 2007;306(1):82–93.
- [10] Voura EB, Jaiswal JK, Mattoussi H, Simon SM. Tracking metastatic tumor cell extravasation with quantum dot nanocrystals and fluorescence emission-scanning microscopy. *Nat Med* 2004;10(9):993–8.
- [11] Cahill KS, Gaidosh G, Huard J, Silver X, Byrne BJ, Walter GA. Noninvasive monitoring and tracking of muscle stem cell transplants. *Transplantation* 2004;78(11):1626–33.
- [12] Yoneyama R, Chemaly ER, Hajjar RJ. Tracking stem cells in vivo. *Ernst Schering Res Found Workshop* 2006;60:99–109.
- [13] Zhang SJ, Wu JC. Comparison of imaging techniques for tracking cardiac stem cell therapy. *J Nucl Med* 2007;48(12):1916–9.
- [14] Hoshino K, Ly HQ, Frangioni JV, Hajjar RJ. In vivo tracking in cardiac stem cell-based therapy. *Prog Cardiovasc Dis* 2007;49(6):414–20.
- [15] Weissleder R, Hahn PF, Stark DD, Elizondo G, Saini S, Todd LE, et al. Superparamagnetic iron oxide: enhanced detection of focal splenic tumors with MR imaging. *Radiology* 1988;169(2):399–403.
- [16] Weissleder R, Elizondo G, Wittenberg J, Rabito CA, Bengele HH, Josephson L. Ultrasmall superparamagnetic iron oxide: characterization of a new class of contrast agents for MR imaging. *Radiology* 1990;175(2):489–93.
- [17] Shapiro EM, Skrtic S, Koretsky AP. Sizing it up: cellular MRI using micron-sized iron oxide particles. *Magn Reson Med* 2005;53(2):329–38.
- [18] Metz S, Bonaterre G, Rudelius M, Settles M, Rummeny EJ, Daldrop-Link HE. Capacity of human monocytes to phagocytose approved iron oxide MR contrast agents in vitro. *Eur Radiol* 2004;14(10):1851–8.
- [19] Montet-Abou K, Montet X, Weissleder R, Josephson L. Cell internalization of magnetic nanoparticles using transfection agents. *Mol Imaging* 2007;6(1):1–9.
- [20] Petri-Fink A, Hofmann H. Superparamagnetic iron oxide nanoparticles (SPIONs): from synthesis to in vivo studies – a summary of the synthesis, characterization, in vitro, and in vivo investigations of SPIONs with particular focus on surface and colloidal properties. *IEEE Trans Nanobioscience* 2007;6(4):289–97.
- [21] Matuszewski L, Persigehl T, Wall A, Schwindt W, Tombach B, Fobker M, et al. Cell tagging with clinically approved iron oxides: feasibility and effect of lipofection, particle size, and surface coating on labeling efficiency. *Radiology* 2005;235(1):155–61.
- [22] Lewin M, Carlesso N, Tung CH, Tang XW, Cory D, Scadden DT, et al. Tat peptide-derivatized magnetic nanoparticles allow in vivo tracking and recovery of progenitor cells. *Nat Biotechnol* 2000;18(4):410–4.
- [23] Arbab AS, Yocum GT, Kalish H, Jordan EK, Anderson SA, Khakoo AY, et al. Efficient magnetic cell labeling with protamine sulfate complexed to ferumoxides for cellular MRI. *Blood* 2004;104(4):1217–23.
- [24] Tai JH, Foster P, Rosales A, Feng B, Hasilo C, Martinez V, et al. Imaging islets labeled with magnetic nanoparticles at 1.5 Tesla. *Diabetes* 2006;55(11):2931–8.
- [25] Walczak P, Kedziora DA, Gilad AA, Lin S, Bulte JW. Instant MR labeling of stem cells using magnetoelectroporation. *Magn Reson Med* 2005;54(4):769–74.
- [26] Shapiro EM, Skrtic S, Sharer K, Hill JM, Dunbar CE, Koretsky AP. MRI detection of single particles for cellular imaging. *Proc Natl Acad Sci U S A* 2004;101(30):10901–6.
- [27] de Vries IJ, Lesterhuis WJ, Barentsz JO, Verdijk P, van Krieken JH, Boerman OC, et al. Magnetic resonance tracking of dendritic cells in melanoma patients for monitoring of cellular therapy. *Nat Biotechnol* 2005;23(11):1407–13.
- [28] Shapiro EM, Medford-Davis LN, Fahmy TM, Dunbar CE, Koretsky AP. Antibody-mediated cell labeling of peripheral T cells with micron-sized iron oxide particles (MPIOs) allows single cell detection by MRI. *Contrast Media Mol Imaging* 2007;2(3):147–53.
- [29] Oude Engberink RD, van der Pol SM, Dopp EA, de Vries HE, Blezer EL. Comparison of SPIO and USPIO for in vitro labeling of human monocytes: MR detection and cell function. *Radiology* 2007;243(2):467–74.
- [30] Foster-Gareau P, Heyn C, Alejski A, Rutt BK. Imaging single mammalian cells with a 1.5 T clinical MRI scanner. *Magn Reson Med* 2003;49(5):968–71.
- [31] Shapiro EM, Sharer K, Skrtic S, Koretsky AP. In vivo detection of single cells by MRI. *Magn Reson Med* 2006;55(2):242–9.
- [32] Song M, Moon WK, Kim Y, Lim D, Song IC, Yoon BW. Labeling efficacy of superparamagnetic iron oxide nanoparticles to human neural stem cells: comparison of ferumoxides, monocrySTALLINE iron oxide, cross-linked iron oxide (CLIO)-NH<sub>2</sub> and tat-CLIO. *Korean J Radiol* 2007;8(5):365–71.
- [33] Shen T, Weissleder R, Papisov M, Bogdanov A, Brady TJ. MonocrySTALLINE iron-oxide nanocompounds (Mion) – physicochemical properties. *Magn Reson Med* 1993;29(5):599–604.
- [34] Pittet MJ, Swirski FK, Reynolds F, Josephson L, Weissleder R. Labeling of immune cells for in vivo imaging using magnetofluorescent nanoparticles. *Nat Protoc* 2006;1(1):73–9.
- [35] Zhao M, Kircher MF, Josephson L, Weissleder R. Differential conjugation of tat peptide to superparamagnetic nanoparticles and its effect on cellular uptake. *Bioconjug Chem* 2002;13(4):840–4.
- [36] Ayyub P, Palkar VR, Chattopadhyay S, Multani M. Effect of crystal size-reduction on lattice symmetry and cooperative properties. *Phys Rev B* 1995;51(9):6135–8.
- [37] Solomon I. Relaxation processes in a system of two spins. *Phys Rev* 1955;99:559.
- [38] Bloembergen N. Proton relaxation times in paramagnetic solutions. *J Chem Phys* 1957;27(2):572–3.
- [39] Giljohann DA, Seferos DS, Patel PC, Millstone JE, Rosi NL, Mirkin CA. Oligonucleotide loading determines cellular uptake of DNA-modified gold nanoparticles. *Nano Lett* 2007;7(12):3818–21.
- [40] Duncan R, Izzo L. Dendrimer biocompatibility and toxicity. *Adv Drug Deliv Rev* 2005;57(15):2215–37.
- [41] Foged C, Brodin B, Frokjaer S, Sundblad A. Particle size and surface charge affect particle uptake by human dendritic cells in an in vitro model. *Int J Pharm* 2005;298(2):315–22.
- [42] Chung TH, Wu SH, Yao M, Lu CW, Lin YS, Hung Y, et al. The effect of surface charge on the uptake and biological function of mesoporous silica nanoparticles 3T3-L1 cells and human mesenchymal stem cells. *Biomaterials* 2007;28(19):2959–66.
- [43] Luo D, Saltzman WM. Synthetic DNA delivery systems. *Nat Biotechnol* 2000;18(1):33–7.
- [44] Shi XY, Wang SH, Sun HP, Baker JR. Improved biocompatibility of surface functionalized dendrimer entrapped gold nanoparticles. *Soft Matter* 2007;3(1):71–4.
- [45] Malik N, Wiwattanapatapee R, Klopsch R, Lorenz K, Frey H, Weener JW, et al. Dendrimers: relationship between structure and biocompatibility in vitro, and preliminary studies on the biodistribution of I-125-labelled polyamidoamine dendrimers in vivo. 2000;65:133. *J Control Release* 2000;68(2):299–302.

**Comparative analysis of nanoparticle-antibody  
conjugations: carbodiimide versus click chemistry**

Daniel L.J. Thorek, Drew R. Elias, and Andrew Tsourkas\*

Department of Bioengineering, University of Pennsylvania, Philadelphia, PA 19104

\*Address for correspondence:

Andrew Tsourkas  
Department of Bioengineering  
University of Pennsylvania  
240 Skirkanich Hall  
210 S. 33<sup>rd</sup> Street  
Philadelphia, PA 19104  
[atsourk@seas.upenn.edu](mailto:atsourk@seas.upenn.edu)  
Phone: (215)898-8167  
Fax: (215)573-2071

Running Title: Carbodiimide vs. Click Coupling Reactions

Keywords: Nanoparticles, click, carbodiimide, conjugation, iron oxide

Abbreviations:

Nanoparticles: NPs

Superparamagnetic iron oxide: SPIO

Magnetic resonance: MR

## **Abstract**

The ability to modify the physical, chemical, and biological properties of nanoparticles has led to their use as multi-functional platforms for drug delivery and diagnostic imaging applications. Typically, these applications involve functionalizing the nanoparticles with targeting agents. Antibodies remain an attractive choice as targeting agents because of their large epitope space and high affinity; however, implementation of antibody-nanoparticle conjugates are plagued by low coupling efficiencies and the high cost of reagents. Click chemistry may provide a solution to this problem with reported coupling efficiencies nearing 100%. While click chemistries have been used to functionalize nanoparticles with small molecules, they have not previously been used to functionalize nanoparticles with antibodies. Concerns associated with extending this procedure to antibodies are that reaction catalysts or the ligands required for cross-linking may result in loss of functionality. Here, we evaluated the efficiency of conjugations between antibodies and superparamagnetic iron oxide nanoparticles using click chemistry as well as the functionality of the product. Results were compared with conjugates formed through carbodiimide cross-linking. The click reaction allowed for a higher extent and efficiency of labeling compared with carbodiimide, thus requiring less antibody. Further, conjugates prepared via the click reaction exhibited improved binding to target receptors.

## Introduction

Nanoparticles (NPs), commonly defined as organic or inorganic materials with at least one length dimension below 100 nm, are being widely investigated as drug delivery vehicles and/or imaging agents. Interest in NPs largely stems from their ability to carry a large therapeutic payload (or ample amounts of contrast agent), the ability to finely tune physicochemical properties, which can influence their pharmacokinetic and pharmacodynamic profiles, and the ability to functionalize their surface with molecularly specific targeting agents. For both diagnostic (1) and therapeutic (2) applications, it is becoming increasingly recognized that specific targeting of NPs is critical towards their effective use. When targeted, reduced amounts of therapeutic and imaging agents are required compared with systemically delivered vectors (3). Furthermore, targeting greatly reduces nonspecific background signal from accumulation of contrast agents at undesirable sites. This also leads to lower toxicity and improved efficacy of therapeutics.

Superparamagnetic iron oxide nanoparticles (SPIO) are a widely used NP system affording  $T_2^*$ -weighted contrast for magnetic resonance (MR) imaging applications (4). Recently, SPIO have been conjugated to a variety of targeting ligands to provide cellular and molecular specificity for in vitro diagnostic (5) and in vivo imaging (6) applications. Strategies for targeting SPIO include the use of peptides, endogenous ligands and monoclonal antibodies (7-9). Despite their relatively large size (roughly 150 kDa), antibodies remain an attractive choice because of their combinatorially large epitope space (of approximately  $10^{15}$ ) and their high affinity for targets, with  $K_d$ 's often on the order of nM (10).

Currently, one of the biggest obstacles faced with the use of antibodies is their low conjugation efficiency to NPs, which can result in the need for large quantities of antibody and prohibitive costs (11). One example of a common approach used for conjugation of antibodies to NPs involves carbodiimide cross-linking (12). The zero length cross-linker 1-ethyl-3-(3-dimethylaminopropyl) carbodiimide hydrochloride (EDC) reacts with carboxylated NPs in the presence of sulfo-N-hydroxysuccinimide (sulfo-NHS) to form amine-reactive sulfo-NHS esters. Subsequent addition of antibodies results in coupling between the NPs and primary amines on the antibody via a stable amide bond. Unfortunately, the reaction is non-ideal as it is highly inefficient and thus requires a high excess of antibody. Typically, only about 1-20% of the antibody used during the conjugation procedure will be coupled to the NP (9, 13, 14).

Recently, the emergence and adoption of click chemistry has had a large impact in drug discovery and materials synthesis due to the ability to achieve conjugation efficiencies nearing 100%. The rapid rise of click chemistry is evident from its novel use in a variety of disciplines including medicinal chemistry (15), materials and polymer science (16, 17) and molecular imaging (18, 19). Click chemistry refers to modular chemical conjugations with an emphasis on simple reactions that can take place under a range of conditions with stereospecificity and high efficiency (20). The most widely adopted reaction of this type, the  $Cu^I$ -catalyzed terminal alkyne-azide cycloaddition (CuAAC), was developed by the Sharpless and Meldal groups independently in 2002 (21, 22).

Previously, it has been shown that the coupling of low molecular weight species such as peptides (23) and fluorophores (5) to SPIO can be accomplished with CuAAC. However, evidence that functional antibodies can be coupled to SPIO through CuAAC is lacking. Likewise, reference of large protein linkage to any NP system using a click approach is scarce. Gupta et al. have briefly described holo-transferrin bound viral capsids, although this was reported by way of TEM (transmission electron microscopy) micrographs (24). Lipases have also been

conjugated to gold nanoparticles; (25) however, these enzymes are significantly smaller (~5 times) than antibodies. Applications where two large molecules/nanoparticles must be coupled is where efficient conjugation is needed most, especially when one of the biological species is available in limited quantities and/or is expensive, as is typically the case with antibodies.

A major concern with using CuAAC for NP-antibody coupling reactions is that the antibodies will be irreversibly degraded and/or modified during the reaction. For example, it has previously been shown that the CuAAC reaction can result in the irreversible degradation of viral capsids (26) and nucleic acids (27). Further, antibodies could become non-functional due to modification of the innate protein with click reactive ligands.

In this work we evaluated the use of CuAAC for conjugation of SPIO to anti-CD20. Anti-CD20 is a clinically approved chimeric monoclonal antibody that has been approved for use in treating B cell lymphoma. This antibody has also been used previously to target SPIO to CD20 expressing tumors (28). We have sought to comparatively assess the utility of the CuAAC reaction for antibody targeting of SPIO against an accepted method, that of carbodiimide conjugation. Particle labeling was assessed for both strategies by means of the efficiency and extent of protein-to-particle labeling and by functional cell-targeting assays.

### **Experimental Procedures**

**Materials:** Azido-dPEG<sub>12</sub> NHS ester and Propargyl-dPEG NHS ester were purchased from Quanta BioDesign Ltd., (Powell, OH). The nanoparticle coating material, dextran T10, was purchased from Amersham Biosciences (now GE Healthcare, Piscataway, NJ). Reagent grade IgG (Immunoglobulin G) from rat serum was acquired from Sigma Aldrich (St. Louis, MO), while anti-CD20 antibody, Rituximab, (Genentech, South San Francisco, CA) was a gift of the Eisenberg group. Human lymphoma B cells (Burkitt GA-10) were obtained from ATCC (Manassas, VA). Bathocuproinedisulfonic acid (BCS) was acquired from Acros Organics (Geel, Belgium). All other reagents were purchased from Thermo Fisher Scientific, (Waltham, MA), unless otherwise noted.

**SPIO Synthesis and Amination:** SPIO were prepared by chemical co-precipitation, as previously described (29). Briefly, 0.7313 g FeCl<sub>2</sub> and 1.97 g FeCl<sub>3</sub> were each dissolved in 12.5 mL diH<sub>2</sub>O and added to 25 g dextran T10 in 50 mL diH<sub>2</sub>O at 4°C. Ammonium hydroxide (15 mL) was slowly added to this mixture turning the light yellow colored solution black. This nanoparticle slurry was then heated to 90°C for 1 h and cooled overnight.

Purification of SPIO was accomplished by ultracentrifugation of the mixture at 20K RCF (relative centrifugal force) for 30 min. Pellets were discarded and the supernatant was subjected to diafiltration against greater than 20 volumes of 0.02 M citrate, 0.15 M sodium chloride buffer, using a 100 kDa cutoff membrane filter (GE Healthcare). The purified particles were then cross-linked by reacting the particles (10 mg Fe/mL) with 25% (v/v) 10 M NaOH and 33% epichlorohydrin. After mixing for 24 h, the particles were briefly dialyzed and then functionalized with amines by adding 25% ammonium hydroxide. This reaction was allowed to continue for another 24 h followed by diafiltration as above.

**SPIO Characterization:** The hydrodynamic diameter of the nanoparticles was measured using a Zetasizer Nano-z (Malvern Instruments, Malvern, UK) through dynamic light scattering (DLS). SPIO particles were diluted in PBS to a concentration of approximately 0.5 mg Fe/mL and read in triplicate. The values reported for all samples are the intensity peak values.



The longitudinal ( $R_1$ ) and transverse ( $R_2$ ) relaxivity of each particle was calculated as the slope of the curves  $1/T_1$  and  $1/T_2$  against iron concentration, respectively.  $T_1$  and  $T_2$  relaxation times were determined using a Bruker mq60 MR relaxometer operating at 1.41 T (60 MHz).  $T_1$  measurements were performed by collecting 12 data points from 5.0 to 1000 msec with a total measurement duration of 1.49 minutes.  $T_2$  measurements were made using  $\tau = 1.5$  msec and 2 dummy echoes, and fitted assuming a monoexponential decay.

The number of amines per particle was determined following the general procedure described by Zhao et al. (30). Briefly, iron oxide particles at a concentration of 2 mg Fe/mL were reacted with excess N-Succinimidyl 3-(2-pyridyldithio) propionate (SPDP, Calbiochem, San Diego, CA) for 4 hours. SPIO were washed of excess SPDP through repeated precipitation in isopropanol and resuspension in PBS. The particles were then run through a 50 kDa MWCO centrifugal filter (YM-50, Millipore, Billerica, MA) either with or without the addition of disulfide cleavage agent TCEP. The difference of the absorbance of these two samples at 343 nm was used to determine the concentration of SPDP in the filter flow. Adjusting for dilution, the number of amines per particle was determined.

FITC Modification of SPIO: Fluorescein-isothiocyanate (FITC) was used to fluorescently label amine-functionalized cross-linked SPIO by reacting at a molar ratio of 19:1 FITC to iron. The unbound FITC was washed from the FITC-SPIO using a PD10 gel filtration column (GE Healthcare) equilibrated with phosphate buffered saline (PBS). All particles were FITC-labeled prior to subsequent modification, ensuring that all particles had equal fluorescent labeling.

Carboxylation of SPIO: A schematic outlining the carbodiimide crosslinking procedure is illustrated in Figure 1A (strategy i). FITC labeled, amine-functionalized NPs (as shown in Figure 1B) were derivatized to acid residues following reaction with an excess of succinic anhydride in basic solution. Specifically, 200  $\mu$ L of  $\text{NH}_2$ -SPIO (5 mg Fe/mL) in 0.02M citrate buffer, pH 8 was added to 10  $\mu$ L of 1 M NaOH followed by 10  $\mu$ L of 4 M succinic anhydride in DMF. The reaction was allowed to mix for 4 hours. Carboxylated-SPIO (COOH-SPIO) were subsequently precipitated three times in 4 volumes of isopropanol to remove free reactants.

Carbodiimide Conjugations: Carbodiimide coupling reactions were accomplished with FITC labeled COOH-SPIO in 2-(N-morpholino)ethanesulfonic acid (MES) buffer, pH 6.0. To 50  $\mu$ L of SPIO (2 mg Fe/mL), 10  $\mu$ L each of 200 mM EDC and 500 mM sulfo-NHS was added. Solutions mixed for one hour at 25°C, were then precipitated in 500  $\mu$ L of isopropanol. A resuspension of the NPs in 100  $\mu$ L of 10 mg/mL antibody solution in PBS, pH 7.4 was allowed to react at 15°C overnight. Purification was carried out using a MS magnetic column (Miltenyi Biotec, Bergisch Gladbach, Germany) in PBS.

The BCA Protein Assay was used for protein concentration of conjugate solutions, after correcting for background with unlabeled SPIO. To determine number of protein per particle, the molarity of SPIO was assessed spectrophotometrically by dissolving the NPs and oxidizing the iron with 6M HCl and 3%  $\text{H}_2\text{O}_2$ . Absorbance at 410 nm was compared to a standard curve and particle concentration was calculated assuming 8924 Fe atoms per particle, as previously determined (29).

Azide Modification of SPIO: A schematic outlining the CuAAC crosslinking procedure is found in Figure 1A (strategy ii). FITC-SPIO was reacted with the amine-reactive azido-dPEG<sub>12</sub> NHS, diluted 10 times from stock in dimethyl sulfoxide (DMSO), in 0.1 M sodium phosphate buffer, pH 9. The linker was added at 100 times molar excess to the SPIO. After mixing for 4 h, the SPIO

were purified twice on PD10 columns equilibrated with PBS. Azide-SPIO was then concentrated on an Ultracel 30k centrifugal filter (Millipore, Billerica, MA) in PBS.

Alkyne Functionalization of Antibodies: Alkyne functionalization of antibodies (Figure 1C), for both IgG and Rituximab, was accomplished by addition of 10% v/v propargyl-dPEG-NHS in DMSO to 10 mg/mL antibody in 0.1M sodium phosphate buffer, pH 9. The concentration of propargyl-dPEG-NHS was varied to provide different degrees of labeling per antibody. Antibody was purified on a PD10 column equilibrated with PBS and then re-concentrated using Ultracel 30k filters. Antibody concentration post-purification was assessed spectrophotometrically at 280 nm using a molar extinction coefficient of  $210000 \text{ M}^{-1}\text{cm}^{-1}$ .

CuAAC Conjugation: SPIO was conjugated to alkyne functionalized IgG and anti-CD20 using the same procedures. FITC labeled  $\text{N}_3$ -SPIO (3 mg Fe/mL) was mixed with varying volumes of 10 mg/mL alkynated-antibody, 5 mM BCS, 1 mM  $\text{CuSO}_4$  and 5 mM sodium ascorbate. Final volumes of the reactions were brought to a constant level with the addition of PBS. The samples were mixed for 4 h at  $15^\circ \text{C}$ . Samples were cleaned of the reaction additives using an YM-50 spin column. The antibody-linked nanoparticles were then purified from unbound protein on a MS magnetic column. Protein per particle labeling was determined as above.

Cell Labeling and Assessment: SPIO were incubated with  $100 \mu\text{L}$  of  $1 \times 10^6$  cells/mL Burkitt's GA-10 lymphoma B cells for 30 minutes at  $37^\circ \text{C}$ , 5 %  $\text{CO}_2$  in a 96 well plate. SPIO were added at final concentrations of  $50 \mu\text{g Fe/mL}$  and  $10 \mu\text{g Fe/mL}$  for carbodiimide- and click-conjugated SPIO, respectively. In the antibody inhibition experiments,  $50 \mu\text{g/mL}$  (final concentrations) of free anti-CD20 was added prior to the addition of the antibody-conjugated nanoparticles. The free, unbound particles, were purified from the cells through three PBS washes at 1 RCF for 5 minutes each. Cells were finally resuspended in  $300 \mu\text{L}$  of PBS and placed in a 96-well plate to be read using a Guava Easycyte Plus system (Guava Technologies, Hayward, CA). Flow cytometry data was analyzed using FlowJo (TreeStar Inc., San Francisco, CA).

Fluorescent Imaging: Click-conjugated particles at a concentration of  $50 \mu\text{g Fe/mL}$  were incubated with cells as above, using  $30 \times 10^3$  cells. Images were acquired with an Olympus IX 81 inverted fluorescence microscope using a LUC PLAN 40x objective (NA 0.6; Olympus) following fluorescein excitation by and an X-cite 120 excitation source (EXFO, Quebec, QC). Micrographs were taken using a back-illuminated EMCCD camera (Andor Technology PLC, Belfast, Northern Ireland).

## Results and Discussion

Antibodies were coupled to SPIO using either conventional carbodiimide chemistry or CuAAC, as shown in Figure 1A. The SPIO used throughout the present study possessed an average hydrodynamic diameter of 33.4 nm and R1 and R2 values of 13.56  $1/\text{mM} \cdot \text{sec}$  and 71.00  $1/\text{mM} \cdot \text{sec}$ , respectively. The SPIO were also aminated ( $\sim 185 \text{ NH}_2$  per particle), making this probe well suited to modification with dye and proteins. Initially, all CuAAC conjugations were carried out using rat IgG so that the reaction parameters could be optimized in a cost-effective manner. The first parameter to be varied was the number of alkyne groups introduced onto IgG. This was accomplished by varying the labeling ratio of alkynating reagent, CH-PEG-NHS, to IgG from 15:1 to 100:1. In a separate reaction, azide-labeled SPIO was prepared by reacting aminated SPIO with a 100-fold molar excess of  $\text{N}_3$ -PEG-NHS, as seen in Figure 2. Following appropriate purification procedures, alkyne-labeled IgG were coupled to the azide-SPIO through CuAAC in a catalytic copper solution. For this reaction, the molar ratio of IgG per SPIO was held constant at 17.5:1. After a 4 hr incubation, unbound IgG were removed by magnetically

purifying the SPIO and the average number of IgG coupled to each SPIO was quantified. It was found that the number of IgG per SPIO increased with the degree of alkyne incorporation, to a maximum labeling of 10-13 IgG per SPIO for this series of reactions. The maximum number of IgG per SPIO was achieved when IgG was reacted with >35-fold molar excess of CH-PEG-NHS. Therefore, all subsequent alkynating reactions were carried out utilizing these lowest saturating conditions.

An important advantage of CuAAC reactions has been the high efficiency of conjugations. This is a particularly desirable property when procedures involve large and expensive proteins such as antibodies. Next, we determined the conjugation efficiency between IgG and SPIO for labeling ratios of alkyne-IgG to azide-SPIO ranging from 2.5:1 to 35:1. As shown in Figure 3, there was nearly a 100% coupling efficiency when the labeling ratio was less than ~20 IgG per SPIO. At higher labeling ratios, the number of IgG per SPIO did not improve, likely because there was insufficient space on the SPIO surface for additional conjugations. Utilizing this information, subsequent conjugation of the clinically approved anti-CD20 was materially conserved, as a labeling ratio of only 15 antibodies per SPIO was used.

To assess whether antibodies that have been coupled to SPIO remain functionally active following the CuAAC reaction, SPIO were coupled with anti-CD20 antibodies and their ability to bind to CD20-positive B cells was assessed. For comparison, the same antibodies were also coupled to SPIO using carbodiimide chemistry. Each step of the carbodiimide reaction was conducted under saturating conditions to maximize the conjugation efficiency. Specifically, carboxylated SPIO were reacted with an excess of EDC and sulfo-NHS in MES buffer, pH 6.0 for 1 hour in an attempt to achieve complete activation of all available carboxyl groups. To minimize subsequent hydrolysis of the NHS-activated SPIO, unreacted cross-linking agents were removed as rapidly as possible (~2-5 minutes) by precipitating the SPIO with isopropanol. The SPIO were then resuspended directly in an excess of anti-CD20 in PBS, pH 7.4 and mixed overnight.

As shown in Figure 4A, the copper catalyzed ligation of anti-CD20 to SPIO after 4 h yielded approximately 6.85 anti-CD20 per SPIO. Carbodiimide cross-linking only resulted in 2.77 anti-CD20 per SPIO. The labeling efficiency for each conjugation strategy, defined as a percentage of conjugated protein per SPIO over total protein per SPIO is presented in Figure 4B. The click chemistry reaction achieved 45.6% efficiency, while the carbodiimide reaction resulted in a labeling efficiency of only 8.3%. It was surprising that despite a relatively high degree of labeling by the protein through CuAAC, this was significantly less than achieved with rat IgG. It is hypothesized that the reduced efficiency may stem from a lower incorporation of alkynes onto the anti-CD20 compared with IgG, perhaps due to subtle differences between the proteins. Nonetheless, CuAAC still resulted in a 5.5-fold improvement in the efficiency of labeling compared with carbodiimide chemistry.

Binding of anti-CD20-conjugated SPIO to CD20-positive B cells was assessed by flow cytometry. All SPIO were fluorescently labeled prior to the respective conjugation protocols to allow for fluorescence detection. The same fluorescently labeled SPIO were used for both the CuAAC and carbodiimide reactions to ensure that total cellular fluorescence could be directly correlated to the extent of SPIO binding. Thus, it was possible to quantitatively compare between the equally fluorescent EDC- and CuAAC-particle labeling strategies. As shown in Figure 5 (top row), it was found that at a concentration of 10  $\mu$ g Fe/mL, anti-CD20-targeted SPIO prepared using click chemistry could be used to successfully target B cells. Specificity was confirmed by competitively inhibiting SPIO binding using an excess of free anti-CD20

antibodies. Surprisingly, anti-CD20-targeted SPIO prepared using carbodiimide chemistry did not result in any appreciable B cell labeling using equivalent concentrations (10  $\mu\text{g Fe/mL}$ ; D-F). In fact, similar levels of B cell labeling could only be achieved when the iron concentration was increased to 50  $\mu\text{g Fe/mL}$  (Figure 5, bottom row). Again, for both concentrations of the carbodiimide-conjugated targeted nanoparticles, specificity was confirmed by competitively inhibiting SPIO binding using an excess of free anti-CD20 antibodies. This data suggests that the anti-CD20-labeled SPIO prepared using click chemistry have a higher avidity for the CD20 receptors on B cells compared with analogous nanoparticles prepared using carbodiimide chemistry. It is likely that this increase in avidity is due to the greater number of anti-CD20 per particle. Overall, the data presented here provides strong evidence that CuAAC reactions can be used for highly efficient and effective labeling of nanoparticles with antibodies, without any noticeable loss in antibody functionality. Fluorescent micrographs of click conjugated SPIO particles incubated with B cells are also shown (Figure 6). Labeling of the cells is found to be specific, as IgG-SPIO conjugates do not bind to the cells, nor do anti-CD20-SPIO inhibited with excess free antibody.

## **Conclusion**

Advanced applications in the areas of diagnostic imaging and drug delivery stand to benefit from antibody- or protein-based targeting of nanoparticle carriers. Preparation of such targeted nanoparticles can however be inefficient and costly. Here, we have shown that the utilization of the CuAAC for the production of antibody-nanoparticle conjugates permits materially efficient and functionally competent targetable probes. In comparison to classic carbodiimide-conjugates, CuAAC adds a valuable alternative to the toolbox of the bioconjugate chemist. This mechanistically simple and highly efficient reaction, which is generally insensitive to reaction conditions, is expected to allow for an expansion in applications for nanoparticle-targeted systems in the clinic.

## **Acknowledgements**

The authors would like to acknowledge the help of Dr. Eisenberg and his laboratory at the Department of Rheumatology within the School of Medicine at the University of Pennsylvania.

This work was supported in part by Wyeth-Ayerst Pharmaceuticals, the Transdisciplinary Program in Translational Medicine and Therapeutics, the Lupus Research Institute, the DOD Breast Cancer Research Program of the Office of the Congressionally Directed Medical Research Programs (W81XWH-07-1-0457) and the NIH/NCI (R21-CA132658).

## Figure Legends

**Figure 1.** Schematic of Antibody-SPIO Conjugation Strategies. (A) Fluorescently labeled, amine functionalized SPIO were reacted along one of two routes to produce antibody-SPIO conjugates. In strategy (i) carbodiimide chemistry is utilized, following the conversion of the surface amines to COOH groups utilizing succinic anhydride. In strategy (ii), antibody-labeled SPIO are produced by employing Cu<sup>I</sup>-catalyzed terminal alkyne-azide cycloaddition (CuAAC). Azide-modified SPIO are “clicked” to alkyne-labeled antibodies in the presence of copper. (B) Schematic illustrating the preparation of FITC-SPIO. (C) Schematic illustrating the alkyne-PEG modification of antibody, which was necessary for the CuAAC reaction.

**Figure 2.** Effect of IgG alkylation on conjugation to SPIO. To determine the minimally required alkyne residues on IgG necessary to achieve maximum conjugation with SPIO, IgG was reacted with increasing amounts of CH-PEG-NHS. The alkyne-IgG samples were then “clicked” to N<sub>3</sub>-SPIO and the degree of labeling was assessed. The degree of antibody labeling began to plateau at an approximate starting labeling ratio of 35 CH-PEG-NHS:IgG.

**Figure 3.** Efficiency of CuAAC-based IgG-SPIO conjugations as a function of IgG concentration. The click reaction between protein and SPIO was performed with increasing molar excess of IgG to SPIO. The labeling efficiency was ~100% for all conjugations up to a labeling ratio of 20 IgG per SPIO. Higher labeling ratios did not result in any increase in the number of conjugated antibody.

**Figure 4.** Comparison of SPIO labeling with anti-CD20 using CuAAC and carbodiimide conjugation procedures. (A) Following the optimization of IgG-SPIO conjugation using CuAAC, anti-CD20 antibodies were “clicked” to SPIO. The average number of antiCD20 per SPIO was determined by BCA Protein Assay to be 6.85 molecules per particle. Labeling of SPIO by anti-CD20 was also accomplished using the classic carbodiimide method; however a lower final labeling ratio of 2.77 antibodies per SPIO was achieved, despite using more antibodies during the conjugation procedure. (B) The ratio of final protein per NP with respect to the initial amount of protein used during the conjugation reaction has been plotted as a percent. For the CuAAC-mediated crosslinking of anti-CD20 to SPIO, the reaction efficiency approached 50% efficiency, while the efficiency of the EDC reactions approached 10%.

**Figure 5.** B cell labeling with anti-CD20-SPIO. The functional targeting of SPIO to B cells was accomplished for click- and carbodiimide-cross-linked anti-CD20-SPIO conjugates. The top row shows the flow cytometric analysis of B cells that were incubated with 10 µg Fe/mL of CuAAC conjugated (A) IgG-SPIO, (B) anti-CD20-SPIO, and (C) anti-CD20-SPIO in the presence of excess free antibody. Labeling of cells with the corresponding EDC conjugated particles (10 µg Fe/mL) is found in the second row (D-F). B cells labeled with EDC conjugated particles at a higher concentration (50 µg Fe/mL) were analyzed in the final row (G-I). Antibody mediated binding was observed for anti-CD20 SPIO prepared using both conjugation strategies; however, B cell labeling with CuAAC nanoparticles was achieved with a significantly lower concentration of nanoparticles. Solid lines refer to unlabeled B cells. Dashed lines refer to cells incubated with antibody-labeled SPIO of type and concentration indicated by row and column.

**Figure 6.** Fluorescence micrographs of B cells labeled with anti-CD20 SPIO. Cells were incubated for 30 minutes with 50 µg Fe/mL of (A) IgG-SPIO, (B) anti-CD20 SPIO and (C) anti-CD20 SPIO in the presence of excess antibody, and then washed in triplicate. All anti-CD20 SPIO were prepared by CuAAC. The fluorescently labeled particles bind to cells specifically, as

competition for antibody ligand with non-fluorescent anti-CD20 antibodies curtails cell signal. All images are at 40x magnification.

**References:**

1. Helmick L, Antunez de Mayolo A, Zhang Y, et al. Spatiotemporal response of living cell structures in Dictyostelium discoideum with semiconductor quantum dots. Nano Lett. 2008;8:1303-8.
2. Davis ME, Chen ZG, Shin DM. Nanoparticle therapeutics: an emerging treatment modality for cancer. Nat Rev Drug Discov. 2008;7:771-82.
3. Pettit DK, Gombotz WR. The development of site-specific drug-delivery systems for protein and peptide biopharmaceuticals. Trends Biotechnol. 1998;16:343-9.
4. Thorek DL, Chen AK, Czupryna J, Tsourkas A. Superparamagnetic iron oxide nanoparticle probes for molecular imaging. Ann Biomed Eng. 2006;34:23-38.
5. Sun EY, Josephson L, Weissleder R. "Clickable" nanoparticles for targeted imaging. Mol Imaging. 2006;5:122-8.
6. Artemov D, Mori N, Ravi R, Bhujwala ZM. Magnetic resonance molecular imaging of the HER-2/neu receptor. Cancer Res. 2003;63:2723-7.
7. Choi H, Choi SR, Zhou R, et al. Iron oxide nanoparticles as magnetic resonance contrast agent for tumor imaging via folate receptor-targeted delivery. Acad Radiol. 2004;11:996-1004.
8. Kelly KA, Allport JR, Tsourkas A, et al. Detection of vascular adhesion molecule-1 expression using a novel multimodal nanoparticle. Circ Res. 2005;96:327-36.
9. Tsourkas A, Shinde-Patil VR, Kelly KA, et al. In vivo imaging of activated endothelium using an anti-VCAM-1 magnetooptical probe. Bioconjug Chem. 2005;16:576-81.
10. Carter PJ. Potent antibody therapeutics by design. Nat Rev Immunol. 2006;6:343-57.
11. Molday RS, MacKenzie D. Immunospecific ferromagnetic iron-dextran reagents for the labeling and magnetic separation of cells. J Immunol Methods. 1982;52:353-67.

12. Hermanson GT. Bioconjugate Techniques. Hermanson GT, editor. San Diego: Academic Press; 1996.
13. Kocbek P, Obermajer N, Cegnar M, et al. Targeting cancer cells using PLGA nanoparticles surface modified with monoclonal antibody. *J Control Release*. 2007;120:18-26.
14. Natarajan A, Gruettner C, Ivkov R, et al. NanoFerrite particle based radioimmunonanoparticles: binding affinity and in vivo pharmacokinetics. *Bioconjug Chem*. 2008;19:1211-8.
15. Hein CD, Liu XM, Wang D. Click chemistry, a powerful tool for pharmaceutical sciences. *Pharm Res*. 2008;25:2216-30.
16. Lutz JF. 1,3-dipolar cycloadditions of azides and alkynes: a universal ligation tool in polymer and materials science. *Angew Chem Int Ed Engl*. 2007;46:1018-25.
17. Nandivada H, Jiang XW, Lahann J. Click chemistry: Versatility and control in the hands of materials scientists. *Advanced Materials*. 2007;19:2197-208.
18. Baskin JM, Prescher JA, Laughlin ST, et al. Copper-free click chemistry for dynamic in vivo imaging. *Proc Natl Acad Sci U S A*. 2007;104:16793-7.
19. McCarthy JR, Kelly KA, Sun EY, Weissleder R. Targeted delivery of multifunctional magnetic nanoparticles. *Nanomed*. 2007;2:153-67.
20. Kolb HC, Finn MG, Sharpless KB. Click Chemistry: Diverse Chemical Function from a Few Good Reactions. *Angew Chem Int Ed Engl*. 2001;40:2004-21.
21. Rostovtsev VV, Green LG, Fokin VV, Sharpless KB. A stepwise Huisgen cycloaddition process: copper(I)-catalyzed regioselective "ligation" of azides and terminal alkynes. *Angew Chem Int Ed Engl*. 2002;41:2596-9.



22. Tornøe CW, Christensen C, Meldal M. Peptidotriazoles on solid phase: [1,2,3]-triazoles by regiospecific copper(i)-catalyzed 1,3-dipolar cycloadditions of terminal alkynes to azides. *J Org Chem.* 2002;67:3057-64.
23. von Maltzahn G, Ren Y, Park JH, et al. In vivo tumor cell targeting with "click" nanoparticles. *Bioconjug Chem.* 2008;19:1570-8.
24. Sen Gupta S, Kuzelka J, Singh P, et al. Accelerated bioorthogonal conjugation: a practical method for the ligation of diverse functional molecules to a polyvalent virus scaffold. *Bioconjug Chem.* 2005;16:1572-9.
25. Brennan JL, Hatzakis NS, Tshikhudo TR, et al. Bionanoconjugation via click chemistry: The creation of functional hybrids of lipases and gold nanoparticles. *Bioconjugate Chemistry.* 2006;17:1373-5.
26. Wang Q, Chan TR, Hilgraf R, et al. Bioconjugation by copper(I)-catalyzed azide-alkyne [3 + 2] cycloaddition. *J Am Chem Soc.* 2003;125:3192-3.
27. Gierlich J, Burley GA, Gramlich PM, et al. Click chemistry as a reliable method for the high-density postsynthetic functionalization of alkyne-modified DNA. *Org Lett.* 2006;8:3639-42.
28. Baio G, Fabbi M, de Toterò D, et al. Magnetic resonance imaging at 1.5T with immunospecific contrast agent in vitro and in vivo in a xenotransplant model. *Magnetic Resonance Materials in Physics Biology and Medicine.* 2006;19:313-20.
29. Thorek DL, Tsourkas A. Size, charge and concentration dependent uptake of iron oxide particles by non-phagocytic cells. *Biomaterials.* 2008;29:3583-90.
30. Zhao M, Kircher MF, Josephson L, Weissleder R. Differential conjugation of tat peptide to superparamagnetic nanoparticles and its effect on cellular uptake. *Bioconjugate Chemistry.* 2002;13:840-4.



Figure 1.

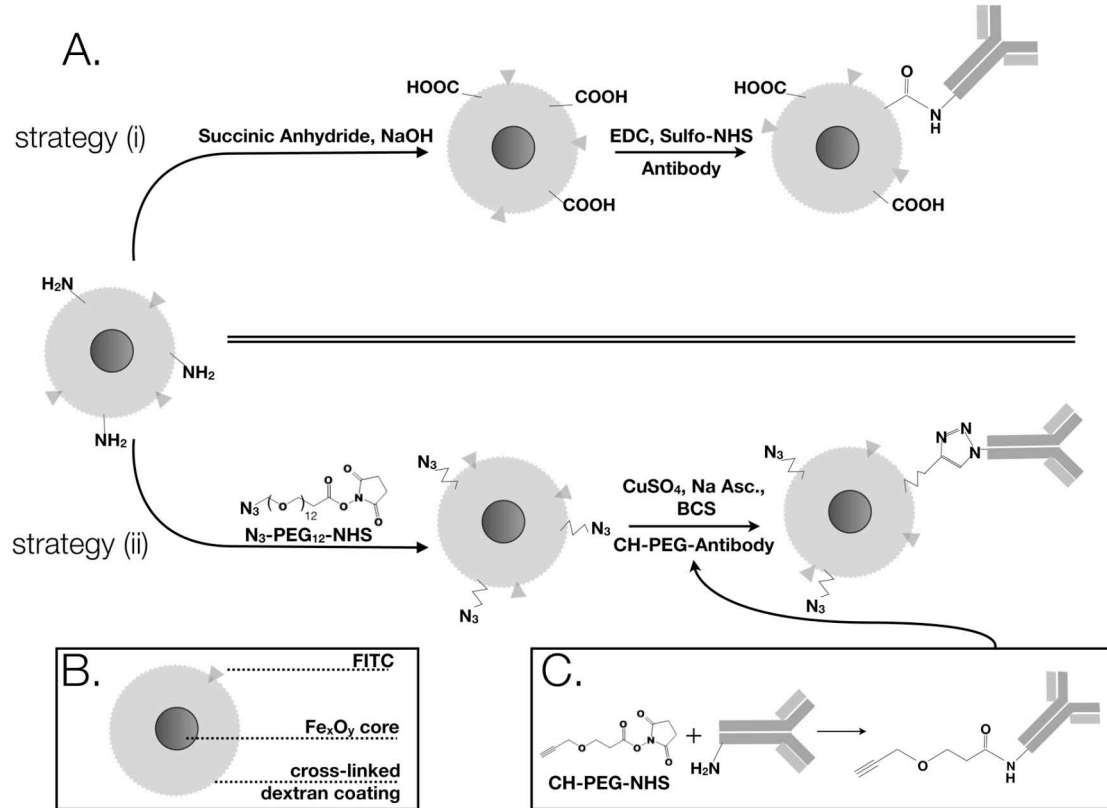


Figure 2.

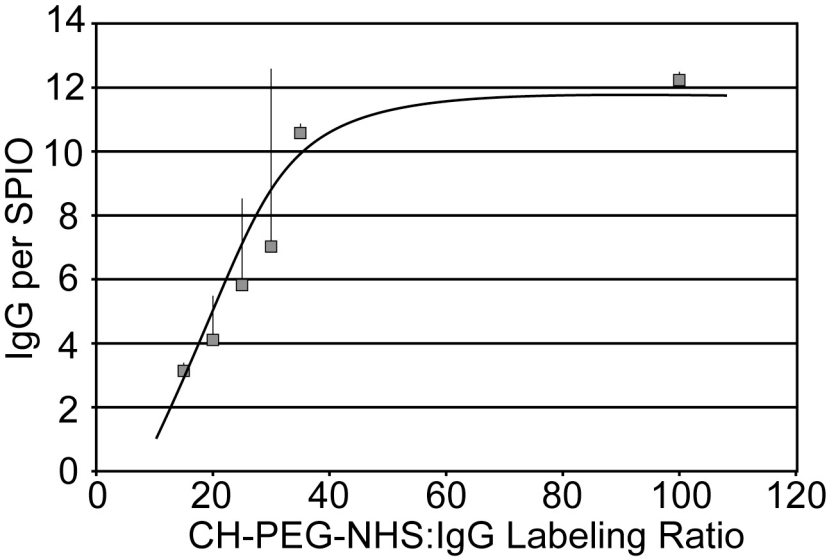


Figure 3.

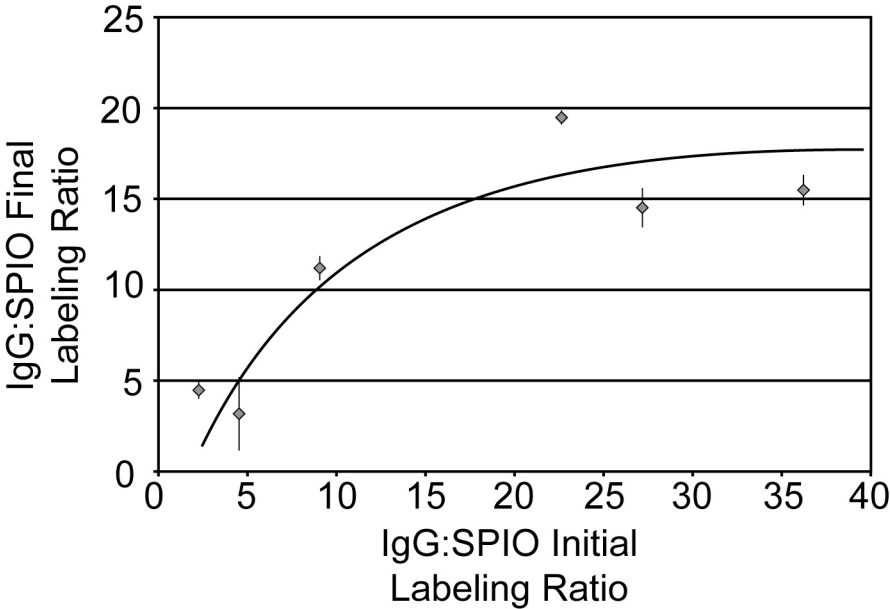


Figure 4.

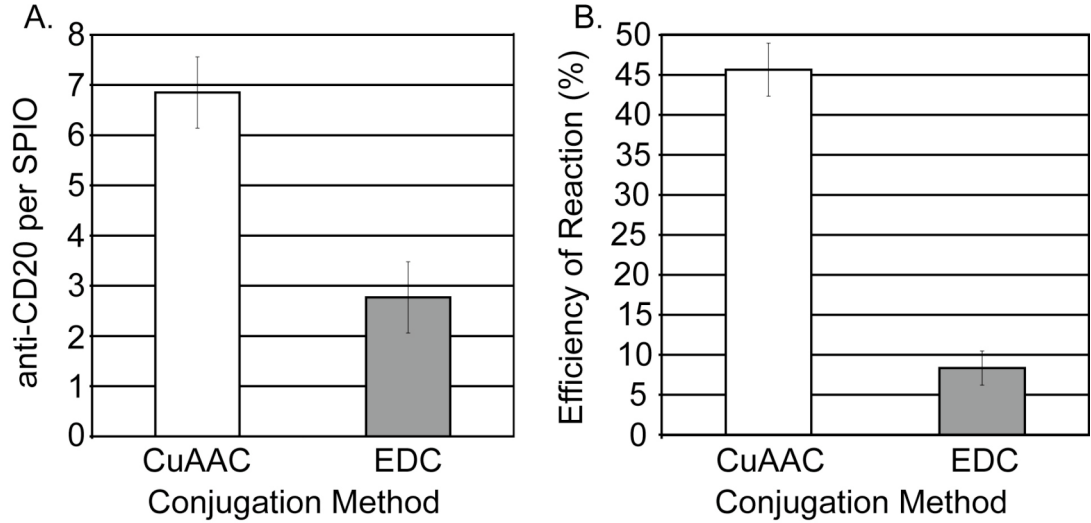


Figure 5.

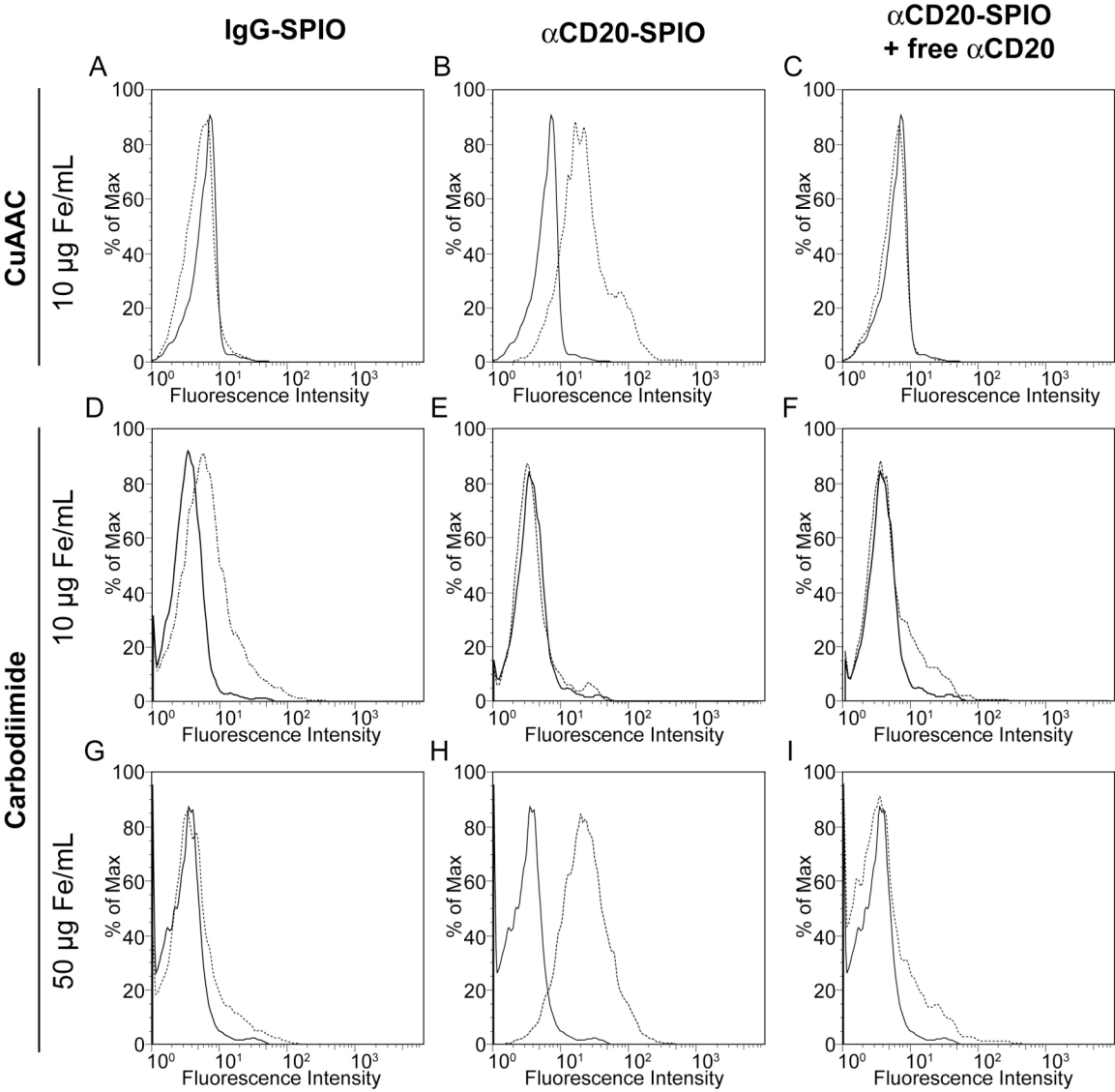


Figure 6.

